Momentum flux characteristics of vertical propagating Gravity Waves

Prosper K. Nyassor[1], Cristiano M. Wrasse[1], Igo Paulino[2], Erdal Yiğit[3], Vera Y. Tsali-Brown[4], Ricardo A. Buriti[2], Cosme A. O. B. Figueiredo[2], Gabriel A. Giongo[1], Fábio Egito[2], Oluwasegun M. Adebayo[1], Hisao Takahashi[1], and Delano Gobbi[1]

[1]Space Weather Division, National Institute of Space Research (INPE), São José dos Campos, Brazil
[2]Academic Unit of Physics, Federal University of Campina Grande (UFCG), Campina Grande, Brazil
[3]Department of Physics and Astronomy, George Mason University, Fairfax, VA, USA
[4]Instituto de Pesquisa e Desenvolvimento (IP&D), Universidade do Vale do Paraíba (UNIVAP), São José dos Campos, Brazil

Correspondence: Prosper K. Nyassor (prosper.nyassor@inpe.br)

Abstract. Momentum flux and propagation dynamics of two vertically propagating atmospheric gravity waves (GW) are studied, using observation at São João do Cariri, Brazil (36.31°W; 07.40°S) by co-located photometer, all-sky imager, and meteor radar. Time series of atomic oxygen green line (OI 557.7 nm), molecular oxygen (O_2 (0 - 1)), sodium D-line (NaD), and hydroxyl (OH (6 - 2)) airglow intensity variations measured by the photometer were used to investigate the vertical characteristics and vertical phase progression of the GWs with similar or nearly the same period across these emission layers. The horizontal parameters of the same GWs were determined from the OH airglow images, whereas the intrinsic parameters of the horizontal and vertical components of the GWs were estimated with the aid of the observed winds. Using the phase of the GWs at each emission layer, the characteristics of the phase progression exhibited near vertical propagations under a duct background propagation condition. This indicates that the duct contributes significantly to the observed near vertical phase propagation. The GW momentum flux and potential energy were estimated using the rotational temperatures of OH and O_2, revealing that the time series of momentum fluxes and potential energies are higher in the O_2 emission than OH, indicating a transfer of momentum and energy across OH to the O_2 altitude. These results reveal the effect of a duct on vertically propagating GW and associated momentum flux and potential energy transfer from the lower to the upper altitudes in the mesosphere.

Copyright statement. TEXT

1 Introduction

The vertical propagation of atmospheric gravity waves (GWs) is known to be the main transport mechanism of momentum and energy into the upper atmosphere (Fritts and Alexander, 2003; Yiğit et al., 2016). Owing to the decrease of density with altitude, amplitudes of GWs increase exponentially if dissipation/wave breaking does not occur. GWs are excited by flows surging up mountains (e.g., Gossard and Hooke, 1975; Lindzen, 1984), fronts and jet streams (e.g., Lindzen, 1984; Fritts and

Alexander, 2003; Wrasse et al., 2024), convective layers (e.g., Townsend, 1966), deep convection / thunderstorms (e.g., Taylor and Hapgood, 1988; Fritts and Alexander, 2003; Sentman et al., 2003; Yue et al., 2009; Vadas et al., 2009; Nyassor et al., 2021, 2022a, b), volcanoes (e.g., Yue et al., 2022; Figueiredo et al., 2023), typhoons (e.g., Li et al., 2022; Chou et al., 2017), by earthquakes (e.g., Heale et al., 2020), solar eclipses (e.g., Paulino et al., 2020, and references therein) and other process that cause imbalance between the gradient of pressure and buoyancy. The waves then propagate both horizontally and vertically (Becker and Schmitz, 2003).

Vertical propagation characteristics of gravity waves are controlled by background temperature and wind relative to the horizontal phase speed of GWs as well as by wave dissipation due to nonlinear diffusion, viscosity, and ion drag (Yiğit et al., 2008, 2021). Depending on wave interaction with the background field, the GWs can be classified as ducted, propagating, or evanescent modes (Gossard and Hooke, 1975). Some of these waves suffer critical level filtering when propagating gravity waves encounter an equal vector of background wind, where the wave can be absorbed by the background (Heale and Snively, 2015). Otherwise, it can be reflected if the gravity wave encounters a strong wind in the opposite direction. According to Fritts and Alexander (2003), reflected GWs from the upper and (or) lower altitude regions can be (partially) ducted. GWs are filtered in the middle and lower thermosphere (MLT) region during breaking. Vertical propagating GWs interact with the mean flow through the transfer of momentum and energy when breaking (Lindzen, 1981; Holton, 1982), particularly in the mesosphere. Thus, these waves significantly contribute to atmospheric circulation and dynamical fields of temperature and wind (Le Du et al., 2022; Yiğit and Medvedev, 2009).

Horizontal and vertical propagation of GWs are greatly influenced by the background wind and temperature fields (Nappo, 2013). The background fields can either hinder or enhance the vertical propagation of GWs. Doppler or thermal ducts favor longer horizontal propagation of GWs (Bageston et al., 2011; Snively et al., 2007; Snively and Pasko, 2008) thereby hindering the vertical propagation. GWs propagating Vertically can either be upward (vertical wavenumber lower than zero, $m < 0$) or downwards ($m > 0$), where energy and momentum are transported in either direction. A typical example is the vertical propagation of secondary GWs which resulted from primary GWs breaking / dissipation in the MLT (Vadas et al., 2003; Medvedev et al., 2023). During the breaking/dissipation of primary GWs, energy and momentum are released, which are further transported upward and downward as they propagate (Vadas et al., 2003).

To study the vertical propagation of GWs, several observational techniques (e.g., Suzuki et al., 2013) have been employed. Observation techniques such as Lidar (Suzuki et al., 2013), radiosonde (Schöch et al., 2004; Sato and Yoshiki, 2008; Yamashita et al., 2009) among others, have been used. In the mesosphere, Nyassor et al. (2018) used an airglow photometer to study the vertical propagation of GWs. According to Nyassor et al. (2018, and references therein), simultaneous observation of multiple airglow emissions is one of the techniques used to investigate the vertical propagation of gravity waves in the mesosphere. This technique is possible if and only if the vertical wavelengths of the waves are larger than the thickness of the airglow emission layer (Nyassor et al., 2018, and references therein). Such observational data can be used to determine the propagation characteristics and amplitude growth of gravity waves (Taori et al., 2005).

Numerous studies (e.g., Fritts et al., 2006; Suzuki et al., 2013; Love and Murphy, 2016; Kaifler et al., 2020) employed some of these observational techniques to explore the subject of dynamics of GWs and their momentum fluxes and potential ener-

gies. Fritts et al. (2006) investigated the momentum fluxes due to GW activities in the MLT region using wind measurement from incoherent scatter radar (ISR) at Arecibo observatory. Using a time resolution of ∼50 minutes, between 71 and 95 km, they quantified GW momentum fluxes profiles. VHF mesosphere - stratosphere - troposphere (MST) radar measurements situated near Davis station (68.5°S, 78.0°E) were used by Love and Murphy (2016) to study the hourly averaged profiles of GW momentum fluxes between 79 and 90 km along the day. Love and Murphy (2016) investigated hourly averages of momentum fluxes of days considered within the period of 14 December 2014 to 6 January 2015 as well as GW intermittency with altitude. Using a co-located observations, Suzuki et al. (2013) investigated the vertical propagation of GWs from the lower to the upper atmosphere at the Arctic Lidar Observatory for Middle Atmosphere Research (ALOMAR) station (69.31°N, 16.01°E). Using the sodium (Na) airglow imager, the horizontal structure of GWs is observed, whereas the ALOMAR Rayleigh/Mie/Raman (RMR) lidar and sodium lidar reveal the two-dimensional vertical structure of GWs between the stratosphere and the lower thermosphere. This coincident observation, permitted the study of horizontal and vertical characteristics of GWs and the momentum flux at the Na airglow altitude. Kaifler et al. (2020), on the other hand, used high temporal and vertical resolution Lidar to study the derived time series absolute momentum fluxes of mountain waves at 40 km and profile of mean and peak of the absolute momentum fluxes between 10 and 80 km.

The above-mentioned works has by far contributed to quantifying the characteristics of the momentum fluxes of GWs and mountain waves (MWs) through statistical and case studies. However, none of these studies explored the aspect of how the momentum fluxes and possibly potential energies would behave under different vertical and horizontal propagation of GWs considering different background conditions. Therefore, the standing question this work addresses is, the behavior of the momentum flux and potential energy of GW under different phase/energy propagations, thus, upward, downward or ducted. Using the vertical phase propagations of GWs, the energy propagation can be determined and subsequently the required parameters (e.g., vertical velocity and wavelength, potential energy, momentum flux e.t.c).

For this, investigation was conducted on the vertical characteristics of GWs with similar or nearly the same period propagating vertically across four (4) airglow emission layers: atomic oxygen green line (OI 557.7 nm), molecular oxygen (O_2 - 864.5 nm), sodium D-line (NaD - 589.0 nm), and hydroxyl (OH) (6 - 2) band. Next is the determination of the phases of the wave at each layer and consequently the phase propagation. The horizontal characteristics of the same GWs are estimated from OH all-sky images. Using observed wind, the intrinsic parameters were also estimated. Having determined and classified these GWs as vertically propagating, the background propagation conditions are studied as well as the potential energy and momentum flux at the OH and O_2. The temperature measurements employed to determine the potential energy and momentum flux were obtained using the rotational temperature at the OH and O_2 emission layers. The dynamics of the GWs potential energy and momentum flux under the determined propagation condition were then studied. It was discovered that the vertical propagation of the cases selected were controlled by the background conditions imposed by the wind and temperature.

2 Observation and data analysis

2.1 Airglow

Airglow is a natural upper atmospheric phenomenon in which light is emitted due to de-excitation of atomic and ionic constituents from higher to lower energy levels. Physical causes of airglow includes chemical reaction of neutral constituents of the upper atmosphere and reactions involving ionized constituents. Though other mechanisms do exist, these two are omnipresent and contribute to the light of the night sky (Roach, 2013). Airglow is among the atmospheric tracers used in the study of atmospheric waves. In this work, the dynamics of GWs in the mesosphere are studied using airglow modulated intensities by GWs in the hydroxyl (OH (6 - 2), hereafter OH), sodium D-line (NaD-Line, hereafter NaD), molecular oxygen (O_2 (0 - 1), hereafter O_2) and atomic oxygen (OI 557.7 nm, hereafter OI 5577) emission layers.

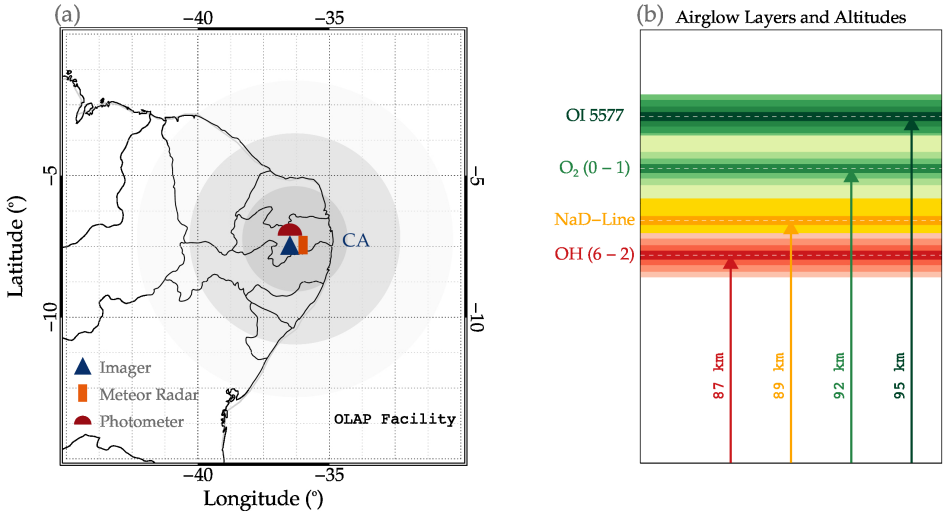

Figure 1. (a) Geographical location of the observatory and co located instruments, as well as the imager field of view at the hydroxyl (OH) airglow layer. The dark blue triangle, orange filled vertical rectangle and red filled semi-circle represent the positions of the all-sky imager (imager), meteor radar and photometer, respectively. The deep gray shaded region indicates a radius of 256 km. The medium gray circular shaded region indicate the field of view of the imager (with a radius of 512 km) whereas the light shaded region shows a radius of 768 km. (b) Airglow emission layers and their respective altitudes. The red, gold, light green, and deep green respectively represent the hydroxyl (OH), sodium D-line (NaD), molecular oxygen atmospheric band (O_2(0 - 1)) and the green line atomic oxygen (OI 5577) emission layers. The respective dark colors with white horizontal dashed lines indicate the peak altitude of each emission layer as indicated by the corresponding labeled vertical arrows.

The peak altitudes of OH, NaD, O_2, and OI 5577 are ∼87 km ($\Delta z = 8$ km), ∼90 ($\Delta z = 8$ km), ∼92 ($\Delta z = 8$ km) and ∼95 km ($\Delta z = 8$ km), respectively. Figure 1(a) shows the location of the Paraíba Atmospheric Luminescence Observatory, in Portugese, Observatório de Luminescência atmosférica da Paraíba (OLAP) where the photometer, all-sky imager (hereafter, imager) and

meteor radar used in this research are hosted. In Figure 1a. The dark blue triangle, orange filled vertical rectangle and red filled semi-circle represent positions of the imager, meteor radar and photometer, respectively. The deep gray shaded region indicates a radius of 256 km. The medium gray circular shaded region indicate the field of view of the imager (with a radius of 512 km), whereas light shaded region shows a radius of 768 km.

The airglow emissions with the peak emission depicted in dark horizontal lines and altitude range (Δz) of each emission layer in their respective faint colors is presented in Figure 1(b). The red, gold, light green, and deep green represent the hydroxyl (OH), sodium D-line (NaD), molecular oxygen atmospheric band (O_2) and the green line atomic oxygen (OI 5577) emission layers, respectively. The respective dark colors with white horizontal dashed lines indicate the peak altitude of each emission layer as indicated by the corresponding labeled vertical arrows. Using instruments such as, airglow photometers and imagers with distinct bandpass filters, each emission layer can be observed. For this work, variations in the airglow intensity of these four emission layers shown in Figure 1(b) are used.

2.1.1 Airglow Photometer

The airglow photometer used in the observation of the mesospheric airglow emissions is located at São João do Cariri (36.31°W; 07.40°S). The photometer is a multi-channel tilting filter photometer (Multi-3) with five interference filters. The background continuum intensity (R nm^{-1}) and the line intensity in Rayleigh (R) were measured to obtain the zenith sky spectrum by tilting the filters relative to their optical axes in which a scan of a wavelength of about 8 nm was made. The mesospheric component of the OI 5577 was estimated by removing the effect of the simultaneous observation of OI 630.0 nm (hereafter, OI 6300) intensity in the ionospheric F-region component computed as 20% (Silverman, 1970). The temporal resolution of the observation is 2 minutes, thus GWs with periods greater than 2 minutes can be observed. The photometer characteristics, that is, calibration scheme and error, spectral resolution, and sensitivity, can be seen in Nyassor et al. (2018, and references therein).

An observation scheme of 13 nights per month centered around the time of new moon was made with more than 6 h of continuous observation time per night. The observational data used for this study extend from January 2000 to December 2007, which resulted in a total of clear sky observation nights of 1051. Details on the Multi-3 filter photometer can be found in Wrasse et al. (2004) and references therein. The database of OI 5577 nm, O_2, NaD - Line, and OH was analyzed to find GWs propagating with similar or nearly the same period in each emission altitude. Among the total nights of clear sky night observation, 389 nights present similar periods in at least two emission layers, of which 24 nights present similar periods in three emission layers. For this study, 2 GW events with the same period in all the 4 emission layers are selected. The photometer is used for airglow intensity observation as well as observation of the rotational temperature of O_2 and OH emission layers (Buriti et al., 2001).

2.1.2 Atmospheric Bands Rotational Temperatures derived from OH (6 - 2) Meinel and O_2 (0 - 1)

The complex rotational band spectrum of the OH and O_2 emission permits the determination of mesospheric temperatures by measuring the intensity distribution between various spectral lines in the bands (Innis et al., 2001). The collision frequency of OH with the neutral atmosphere near 90 km of altitude has been shown to be of the order of $10^4\ s^{-1}$ with a lifetime of the

excited OH being around 3 - 10 ms (Mies, 1974). This indicates that the excited OH molecules in the rotational energy levels are in thermal equilibrium with the atmospheric ambient gas (Sivjee and Hamwey, 1987; Takahashi et al., 1998) and thus, a good proxy for atmospheric temperature studies. The OH rotational line spectra is an open structure with separation of 1 - 2 nm between the lines, which makes it easy to measure individual lines with a low resolution (of $\sim$1 nm) spectrometer. Further, the line intensities of most of the bands are only a function of the rotational temperature. Thus, using two lines from a single band, the rotational temperature can be estimated using the following equation (Mies, 1974):

$$T_{n,m} = \frac{E_{\nu'}(J'_m) - E_{\nu'}(J'_n)}{k_B In\left[\frac{I_n}{I_m}\frac{A(J'_m,\nu'\rightarrow J''_{m+1},\nu'')}{A(J'_n,\nu'\rightarrow J''_{n+1},\nu'')}\frac{2J'_m+1}{2J'_n+1}\right]}, \quad (1)$$

where, $T_{n,m}$ is the rotational temperature estimated from two intensity lines, I_n and I_m, from rotational levels J'_n, J'_m in the upper vibrational level ν', to J''_{n+1}, J''_{m+1} in the lower vibrational level ν''. $E_\nu(J)$ is the energy of the level (J,ν). $A(J'_n,\nu' \rightarrow J''_{n+1},\nu'')$ is the Einstein coefficient, for the transition from J'_n,ν' to J''_n,ν''. k_b is the Boltzmann Constant.

Molecular oxygen also satisfies the local thermal equilibrium (LTE) similar to OH bands, which makes it possible for the estimation of the rotational temperature. O_2 is known to have a lifetime of more that $\sim$10 sec, making it capable of attaining the LTE. The rotational temperature can also be determined using a similar procedure of OH rotational temperature.

2.2 All-Sky Imager

An all-sky imager was used to determine the horizontal component of the GWs observed by the photometer. Images of OH, O_2, OI 5577, and OI 6300 airglow emission layers were taken by this equipment. With regard to this work, only the OH and possibly the O_2 bands airglow images corresponding to the selected coincident photometer observation were used. The airglow all-sky imager is an optical instrument made of a fast fish-eye (f/4) lens, a telecentric lens system, a filter wheel, and a charged coupled device (CCD) camera. The CCD camera has an area of 6.04 cm^2 with a 1024 $\times$ 1024 back-illuminated pixel array of 14 bits per pixel. In order to enhance the signal-to-noise ratio, the images were binned on chip down to a resolution of 512×512. The high quantum efficiency, low dark noise (0.5 electrons $pixel^{-1}s^{-1}$), low readout noise (15 electron rms), and high linearity (0.05 %) of this device enable it to measure airglow emissions (Medeiros et al., 2003; Nyassor et al., 2018).

2.3 Meteor Radar

Background winds from a SKiYMET all-sky interferometric meteor radar with a two-element receiving and three-element transmitting antenna were used to observe mesospheric winds. The meteor radar operates at the same location of the photometer and makes observations between 82 and 98 km. This radar operates at a frequency of 35.24 MHz with a maximum transmitter power of 12 kW. The respective temporal and spatial (vertical) resolutions of this radar are typically 2 h and 3 km. The observation characteristics of the radar have been published elsewhere in Nyassor et al. (2018, and references therein) and Lima et al. (2004).

3 Methodology and Data Analysis

3.1 Photometer Time Series

The methods to obtain the final result of the photometer data include (i) preprocessing, (ii) processing, (iii) estimation of parameters, and (iv) discussion. A graphical demonstration of these procedures is shown in the flowchart in Figure 2.

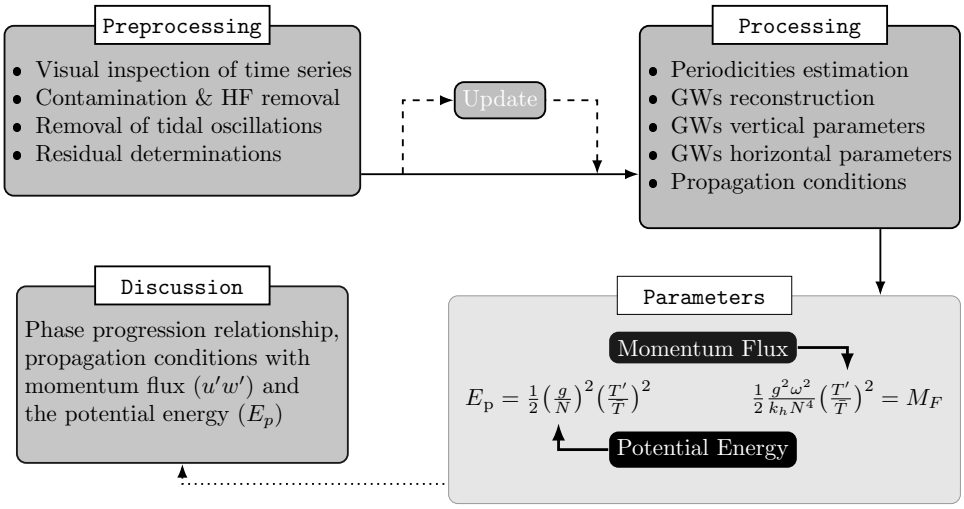

Figure 2. Flowchart showing airglow photometer data processing procedures and GW characterization. The procedure includes preprocessing, processing, parameterization, and discussion.

3.2 Preprocessing

The preprocessing stage involves four steps, as outlined in Figure 2. Firstly, the time series is made up of the variations of wave oscillations and those due to contaminants. Hence, there is a need for visual inspection to detect any of these contaminants that appear as spikes in the time series. The contaminants can be due to artificial light sources, clouds, or astronomical lights moving across the field of view of the photometer. In Figure 3, the hours are in universal time (UT) and span from 18:00 UT on 04 December 2004 to 04:00 UT on 05 December 2004. In Figure 3(a), a typical spike due to contamination is highlighted in light blue background. Also, gaps are usually found in the data due to instrumental problems (however, no gaps exist for this data). A criterion is set such that if the gaps or spikes in the dataset interrupt frequently in order of minutes, the dataset will be disregarded. Spikes are removed from the dataset. If the clean data (data without spikes) has a continuous observation for less than 3 hours, the event of that night is disregarded. Due to the spike (the blue highlighted region) in the time series in Figure 3a, the data is limited to the time interval of 23:00 UT on 04/05/2004 to 03:00 UT on 05/05/2004.

Clean time series with continuous observations of more than 3 hours are considered for further analysis. Next, high frequency oscillations are removed by applying a three-point running mean. Figure 3b shows the clean and smooth (three-point averaged)

data. Finally, to obtain a dataset with only GW oscillations since GWs are modulated by tides, harmonics for semidiurnal and terdiurnal tides are constructed using Equation 2 (red solid line in Figure 3(c)).

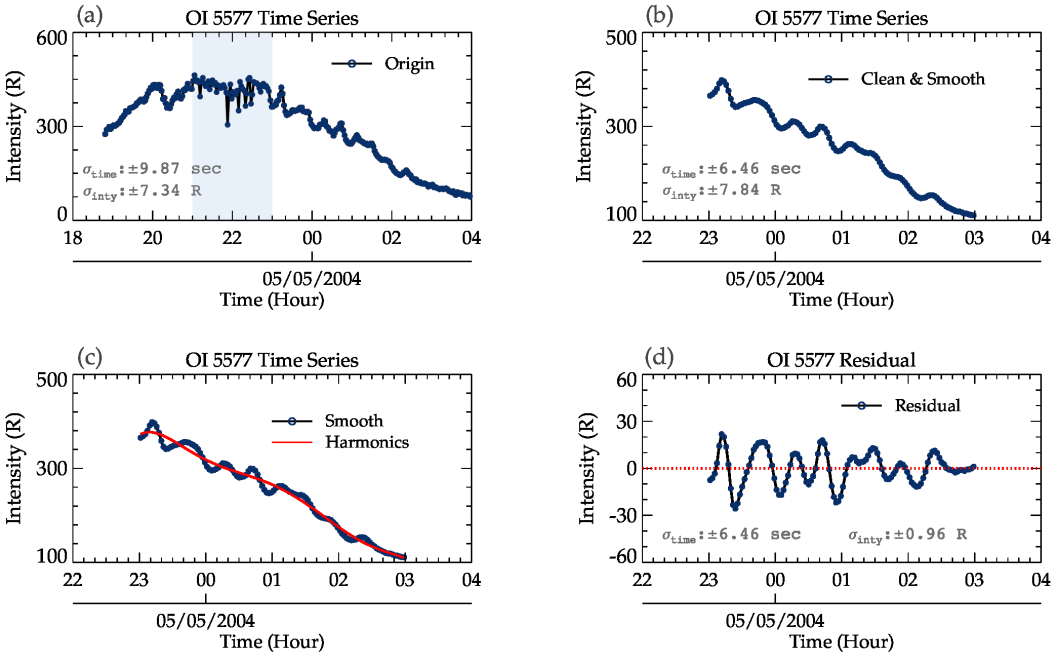

Figure 3. A step-by-step procedure of the preprocessing stage of a photometer data. Panel (a) is the original OI 557.7 nm time series with light blue shaded region indicating the parts of the time series with spikes. In panel (b), the clean and smooth time series is presented. The harmonics of tides, semidiurnal and terdiurnal (red solid line), are constructed and shown in panel (c). The residual (difference between the harmonics and clean-smooth) in (c) is shown in panel (d).

The harmonic is subtracted from the smoothed time series to obtain a time series of the residual (purely GW oscillations). The residual is then used to investigate the vertical propagation of GWs.

$$Y = A + B_i cos\left(\frac{2\pi(x-\phi_i)}{\tau_i}\right) \tag{2}$$

where A and B_i are the unknown amplitudes, x is the observation time series, ϕ_i is the phase, and τ_i is the period. i represent the number of periods, which in this case is the periods of semidiurnal ($\tau = 12\,\mathrm{h}$) and terdiurnal ($\tau = 8\,\mathrm{h}$).

3.3 Processing

In the processing stage, the first step is to inspect if the four emission layers have been modulated by the same GW(s). This is done by plotting the intensity variations. In Figure 4a, the rotational temperature (for OH and O_2) and airglow intensity (for OH, Na D-line, O_2 and OI 5577) variations due to the GW modulations between 23:00 UT on 04/12/2004 and 03:00 UT on

05/12/2004 are presented. The temperature and intensity variations for each emission layer is defined in the respective legends. A similar variation with time was observed in the temperature even though the temperature of the OH was higher than that of O_2. In the case of airglow intensities, well-defined similarities due to the presence of GWs were observed. The variations in the temperature and intensity presented a down-phase progression with time except OH intensity variations.

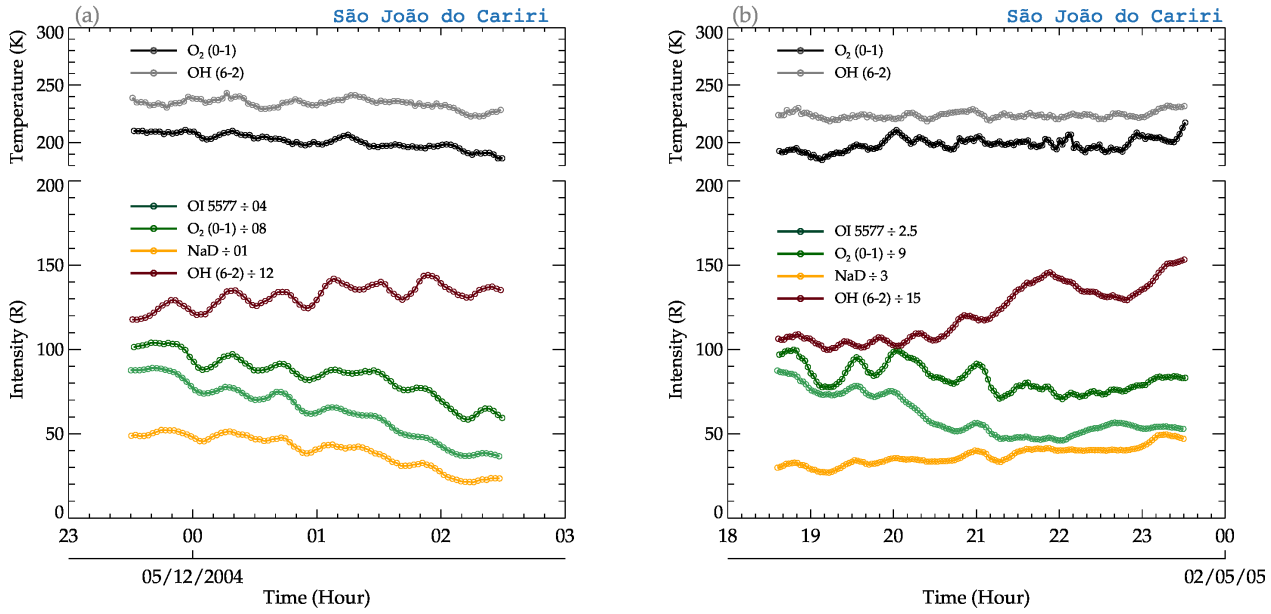

Figure 4. Rotational temperature and airglow intensity variations within 23:00 UT on 04/12/2004 to 03:00 UT on 05/12/2004 (panel a) and 18:30 to 23:30 UT on 01/05/2005 (panel b).

The temperature and intensity variations due to GWs modulation for a second case observed between 18:30 and 23:30 UT on 01/05/2005 is presented in Figure 4b. Similar oscillations can be seen in the variations of the temperatures and the intensities. Unlike the case presented in Figure 4a, the O_2 and OH temperature variations present almost an upward phase progression. Similar characteristics can be found in the variation of the NaD and OH airglow intensities. In contrast, the intensity variations of the OI5577 nm and O_2 present a downward phase progression.

In the processing stage, the residuals were subjected to Lomb-Scargle periodogram and Wavelet analysis to determine the dominant periods in the time series of each emission layer. In Figures 5 and 6, the clean and smoothed time series, residual and the Lomb-Scargle periodogram for all intensities and rotational temperatures of the emission layers for the GW events of 04 - 05/12/2004 and 01/05/2005 are presented, respectively. In panel (a) of Figures 5 and 6, the intensity and temperature time series (similar to Figure 3c) is shown whereas, the residuals are presented in panel (b). The red solid line in panel (a) indicates the tidal harmonics. The subpanels (iii) and (vi) with gray background represent the respective rotational temperatures of O_2 and OH emission as well as their residual and Lomb-Scargle periodogram. Subpanels (i), (ii), (vi), and (v) represent the clean and smoothed, residual and Lomb-Scargle periodogram of OI 5577 nm, O_2, NaD, and OH intensities.

In panel (c) of Figure 5, the Lomb-Scargle periodogram of each intensity and the respective O_2 and OH rotational temperature are presented. As mentioned earlier, at least two similar or nearly the same periods present in each emission layer are selected. The chosen periods are demarcated by vertical dashed lines. It can be seen that almost three similar periods were present, however only two were used in the follow up analysis. This is because the differences in the emission layers are quite large, especially for the OI 5577 emission intensity and the OH rotational temperature.

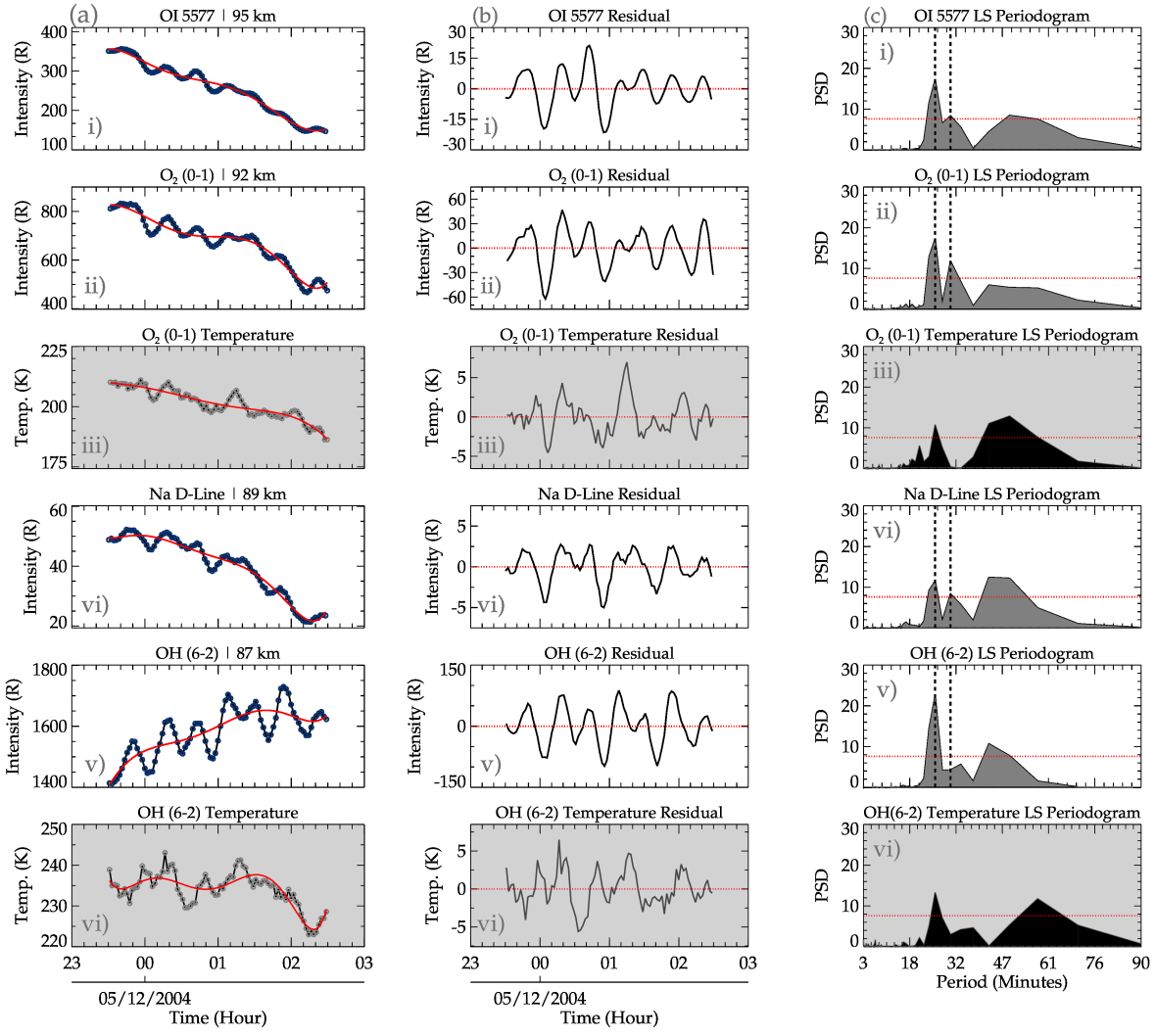

Figure 5. The detailed description of the processing stage of the preprocessed data (obtained form Figure 3). The reconstructed harmonics of the tidal wave oscillations (red solid line) using the dominant periods of 12, and 8 hours and the intensity variations due to GW modulation for each airglow emission layer and those with their rotational temperature are presented in panel (a). The intensity residuals of only GW oscillations are shown in panel (b). In panel (c), the Lomb-Scargle periodogram result of each emission layer intensity and the rotational temperature of O_2 and OH are presented. The red horizontal dotted lines represent 95% significant level.

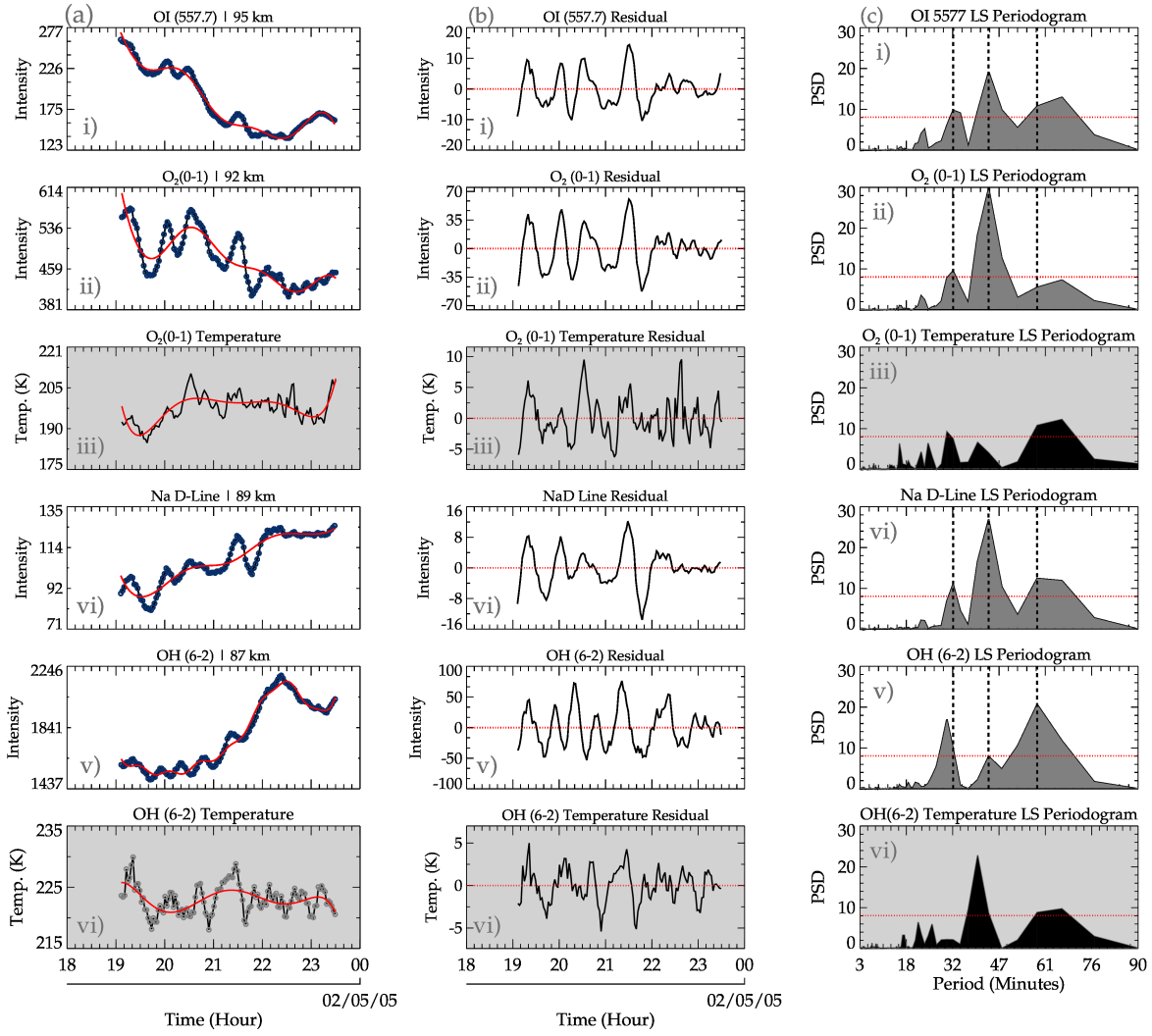

Figure 6. Similar to Figure 5 except for the event of 01/05/2005 between 18:30 and 23:30 UT.

Similar to Figure 5, Figure 6 presents the processing stage of the GW event of 01/05/2005. For this event, the three (3) dominant periods were detected. For the first period, OI, O_2 and NaD present 0.535477 h (32.13 min), whereas, OH $\sim$ 0.503125 h (30.19 h). The second and third dominant periods $\sim$ 0.720896 h (43.25 min) and $\sim$ 1.10274 h (66.16 min), respectively are present in all the emission layers. The periods are indicated by the vertical black dashed lines.

From the above description, at least two dominant peaks are chosen and used to reconstruct new harmonics and over plotted on the residual. The new harmonics is then normalized and plotted in order of increasing altitude, i.e., 87, 89, 92, and 95 km. Note that the rotational temperature of OH (6 - 2) and O_2 were also subjected to the Lomb-Scargle and Wavelet analysis in

order to verify that the temperature was also modulated by the observed GWs in the intensity. From the reconstructed time series and according to their altitude, the phases (ϕ) of the GWs at each altitude were determined.

The phase (ϕ) is estimated from the Equation 2 and is given in decimal hours. However, the phase needs to be estimated considering the start time of the data being used. This is to give the phase in relation to the start time of the time series. This is done by adding the individual dominant period in the time series until it corresponds to the first hour that corresponds to the start time of the data of each emission layer. For instance, the phase of the 04/12/204 OI 5577 nm GW event is 0.0744475 h for GWs with a period of 0.424451 h (∼25.47 min). The phase in this form in relation to the time of observation, thus the period is added to the phase until 23.419253 h (23:25:00 UT) was attained. This is the time corresponding to the first hour of the time series used. A similar procedure was applied to the intensities of the other emissions layers. In Table 1, the result of the phases of the two waves selected for event #01 and three selected waves for event #02 are presented. The phase shifts were determined from the phases determined from each individual emission layers. The phase differences were then estimated between each two consecutive layers as well as the first and the fourth layers.

Table 1. Estimated phases (in hours) in each emission layer of the 04-05/12/2004 and 01/05/2005 GW events. The subscripts τ of ϕ indicate the phase of the corresponding periods.

Events	**Phases ϕ**	**OI**	**O_2**	**NaD**	**OH**
Event #01	$\phi_{\tau=25.24}$ (h)	23.419253	23.417403	23.829630	23.419026
	$\phi_{\tau=38.00}$ (h)	23.259999	23.312784	23.293561	23.683039
Event #02	$\phi_{\tau=31.64}$ (h)	18.880139	18.888510	18.856413	18.844777
	$\phi_{\tau=43.25}$ (h)	18.560785	18.573995	18.565454	18.565454
	$\phi_{\tau=58.43}$ (h)	18.570727	18.548215	18.465382	18.379787

The error associated with each emission layer has been performed to evaluate the impact on the result obtained. The error was assessed by estimating the standard error in the original data, the smoothed data and the harmonics. It is important to mention that the estimated standard error of the mean (σ_M) for OI 5577, O_2, NaD and OH intensities (σ_{M_I}), temperature (σ_{M_T}) and time ($\sigma_{M_{time}}$) are presented in Table 2. The standard errors are estimated for original data, clean and smoothed data, residual and the harmonics.

Table 2. Associated mean standard errors in the time series of the observation hour ($\sigma_{M_{time}}$) in seconds, intensity (σ_{M_I}) in Rayleigh and temperature (σ_{M_T}) in Kelvin for the events of 04/12/2004 and 01/05/2005.

Errors	**Event #01**				**Event #02**			
	OI	**O_2**	**NaD**	**OH**	**OI**	**O_2**	**NaD**	**OH**
Original Data								
$\sigma_{M_{time}}$ (s)	± 09.871	± 09.871	± 09.871	± 09.871	±06.786	±06.786	±06.786	±06.786
σ_{M_I} (R)	±07.339	± 14.745	± 04.076	± 23.243	±03.350	±04.316	±01.110	±18.508
σ_{M_T} (K)		± 01.728		± 03.132		±00.471		±00.186
Usable Data Range								
$\sigma_{M_{time}}$ (s)	± 05.604	± 05.604	± 05.605	± 05.604	±06.786	±06.786	±06.786	±06.786
σ_{M_I} (R)	± 06.958	± 10.911	± 01.052	± 07.998	±03.350	±04.316		±01.110
σ_{M_T} (K)		± 00.670		± 00.413		±00.471		±00.186
Residual								
$\sigma_{M_{time}}$ (s)	± 05.604	± 05.604	± 05.605	± 05.604	±06.786	±06.786	±06.786	±06.786
σ_{M_I} (R)	± 00.964	± 02.537	± 00.203	± 05.024	±00.474	±02.114	±00.410	±02.727
σ_{M_T} (K)		± 00.236		± 00.253		±00.289		±00.172
Harmonics								
σ_{M_H} (R)	± 00.732	± 01.993	± 00.132	± 03.850	±00.411	±01.901	±00.380	±02.256

From Table 2, the estimated errors in the time, intensities and temperature of the original data, clean and smoothed data, residual and the harmonics are presented. In general, the errors associated with the original data is higher than that of the smoothed data and the residual. These values are however, less than the measurement errors of the intensities which is of the order of 5% whereas for rotational temperature, it is 2 - 3 K for O_2 and 4 - 5 K for OH (Wrasse et al., 2004). The error associated with the fit was evaluated by estimating the cross correlation between the time series of the residual of the intensities and temperature and their respective harmonics and are indicated in Figures 7 and 8. The cross correlation of the intensities, that is, their residuals and harmonics are 0.76, 0.79, 0.65 and 0.77 for OI, O_2, NaD and OH intensities, respectively. For the temperature residuals and harmonics for O_2 and OH are 0.52 and 0.67, respectively.

Using the differences in phase and altitude between each of the two consecutive emission layers, the average vertical wavelength (λ_z) of the wave is given by Nyassor et al. (2018)

$$\lambda_z = \frac{V_z}{\tau}, \tag{3}$$

where, $V_z = \Delta d/\Delta\phi$ is the vertical velocity, with Δd being the difference between the higher and lower emission layers and their respective phases denoted by $\Delta\phi$ and τ is the period. A typical result obtained from the procedures in the processing stage is presented in Figure 7 and 8 in Section 4.

3.4 Parameters

In the parameter stage, the potential energy (E_p) and momentum flux ($u'w'$) of the GWs were estimated. The potential energy is estimated using the approach of Narayanan et al. (2024):

$$E_p = \frac{1}{2}\left(\frac{g}{N}\right)^2\left(\frac{T'}{\overline{T}}\right)^2, \tag{4}$$

where, g is the gravitational acceleration, N is the Brunt Väisäla frequency, T' is the GWs perturbations, $\overline{T}$ is the background temperature and T' is the temperature variation due to GW perturbation. The Brunt Väisäla frequency is defined according to Wrasse et al. (2024) as

$$N = \left(\frac{g}{\theta}\frac{d\theta}{dz}\right)^{1/2} \tag{5}$$

and

$$\theta = T\big(P/P_0\big)^{R/c_p} \tag{6}$$

where θ is the potential temperature with p and p_o being pressure and reference pressure, respectively. R is the gas constant, and the c_p is the heat capacity at constant pressure. During this wave event, SABER (Sounding of the Atmosphere using Broadband Emission Radiometry) instrument onboard the TIMED (Thermosphere Ionosphere Mesosphere Energetics Dynamics) satellite, made a passage ∼735 km away from the OLAP observation site. The temperature profiles obtained from the SABER sounding are used in the study of the propagation conditions of each selected GW event of this studies. The measured pressure from SABER observation were used in the determination of the potential temperature and here $K/c_p = 0.286$. Using a first order derivative procedure in interactive data language - IDL (Bowman, 2006), the $d\theta/dz$, profile were determined. The potential temperature at the peak altitude of OH and O_2, which are ∼87 and ∼92 km were chosen. However, the IDL procedure requires three data points to be able to compute the $d\theta/dz$. Since, the temperatures of the OH and O_2 layers are known, the temperature of OI 5577 was inferred from the SABER observation to calculate θ and then used to create a time series (which was kept constant) to attain the required needed input. Thus a constant time series of θ was created for the OI 5577 emission layer.

The zonal and meridional momentum fluxes of the gravity waves is determined by adapting the approach of Suzuki et al. (2007) and Vargas et al. (2009), given by,

$$\begin{aligned} M_{F\,zon} &= \rho_0\langle u'w'\rangle = -\rho_0\frac{1}{2}\frac{km\omega^2}{k_H^2}\frac{g^2}{N^4}\left(\frac{T'}{\overline{T}}\right)^2 \\ M_{F\,mer} &= \rho_0\langle v'w'\rangle = -\rho_0\frac{1}{2}\frac{lm\omega^2}{k_H^2}\frac{g^2}{N^4}\left(\frac{T'}{\overline{T}}\right)^2, \end{aligned} \tag{7}$$

where ρ_0 is the density at the emission layers, $k_H^2 = k^2 + l^2$ is the horizontal wavenumber with k and l being the zonal and meridional wavenumbers, m is the vertical wavenumber, ω is the intrinsic frequency, g is the gravitational acceleration and N the Brunt Väisälä frequency. The density, ρ_0 used in Equation 7 was obtained from SABER sounding close to the observation site during each GW event. The intrinsic frequency ω can be estimated from the expression, $\omega_0 - kU - lV$, where $\omega_0 = 2\pi/\tau$. U and V are the zonal and meridional wind speed in the direction of the wave, respectively, at each peak emission altitude. The horizontal wavenumber, k_H, was estimated from the horizontal wavelength, λ_H, estimated by Equation A5 in Appendix A1, using the relation $k_H = 2\pi/\lambda_H$. The $T'/\overline{T}$ is the relative temperature perturbation, and T' is the GWs induced temperature variation, and $\overline{T}$ is the background temperature. The total momentum flux (M_F) of GW is given by Vargas et al. (2007):

$$M_F = \rho_0 \langle u'w' \rangle = -\rho_0 \frac{1}{2} \frac{g^2}{N^4} \frac{m}{k_H} \omega^2 \left(\frac{T'}{\overline{T}} \right)^2, \tag{8}$$

Estimating the potential energy (E_p) and the momentum flux (M_F) of GWs depends on observed temperature and wind data. As mentioned earlier, rotational temperature from photometer observations were used for M_F and E_p.

3.5 All-Sky Image Pre-Processing and Spectral Analysis

To determine the horizontal parameters of the selected events, images from co-located all-sky imager at São João do Cariri were used. The methodology used for all-sky images processing and GWs parameters estimation implores the validated and updated image pre-processing and spectral analysis (iPreSA) routine of Wrasse et al. (2024), which is capable of pre-processing original airglow images and retrieving GWs horizontal characteristics. The pre-processing aspect includes; (a) the calibration of original images (i.e., to align the image to the geographic coordinates); (b) removal of stars to reduce their effect on the wave spectrum at high frequencies Maekawa (2000); (c) correction of the curvature effect of the charge-coupled device (CCD) camera by mapping the original images onto new coordinates that relate distances between pixels in the image to physical distances in the airglow layer with the zenith at the origin. Other minor corrections implemented in the pre-processing stage involve the estimation of intensity fluctuation fraction, application of high pass filter and weighting function. The current version of the pre-processing also incorporates the correction of Van Rhijn effect and atmospheric extinction, and removal of the milky-way Kubota et al. (2001); Wrasse et al. (2024).

The wave characteristics in the preprocessed airglow images will be obtained using a two-dimensional spectral analysis technique. The underlying concept of this technique is the two-dimensional Discrete Fourier Transform (2D-DFT), represented mathematically as

$$\mathcal{F}(k,l) = \sum_{x=0}^{m-1} \sum_{y=0}^{n-1} \left(c^{-i\frac{2\pi x k}{m}} \right) \left(c^{-i\frac{2\pi y l}{n}} \right) f(x,y) \tag{9}$$

where $\mathcal{F}$(k,l) is the Fourier transform of the function, k, l are the zonal and meridional wavenumbers and $m \times n$ is the dimension of the analyzed image. The cross-spectrum between two successive images is estimated from the amplitude and the phase of the waves. (λ_H), period (τ_H), phase speed (c_H), and propagation direction (ϕ_H). Here, the subscript H indicate horizontal. The

step-by-step description of the spectral analysis of Wrasse et al. (2007), which was used to estimate the horizontal parameters of the observed GWs (Figueiredo et al., 2018; Wrasse et al., 2024) are presented in Appendix A1. From the horizontal wavelength (λ_H), the zonal (k) and meridional (l) wavelength numbers were determined and used in Equations 7 and 8 to estimate the momentum flux. An important condition considered in the selection of the horizontal propagating GWs is that the period must be equal or similar to the period of the vertical component observed in the photometer data. A summary of the keogram-spectral analysis and obtained results are shown in Figures A1, A2, A3, A4 and A5 in Appendix A1.

4 Results

The results of the two (2) selected cases obtained from Section 3 are presented in Figures 7 and 8. Events one (#01) and two (#02) respectively which occurred on 04/12/2004 (4 December 2004) and 01/05/2005 (01 May 2005) at São João do Cariri are presented. To select these cases, they must satisfy the following criteria:

1. GWs with similar or the same periods must be observed in all the four (4) emission layers;
2. similar or the same periods observed in the four airglow intensity variations must be present in the OH and O_2 rotational temperatures and;
3. similar or the same periods observed in criterion #1 must be present in the OH and possibly O_2 all-sky images;
4. the periods of GWs in each emission layer must be present in the time series for 3 hours or more.

Besides selecting these two GW events due to the presence of similar or the same periods in the four emission layers, these events permit the exploration of the dynamics of GWs using (i) observed variables in the MLT region at high temporal resolution and (ii) derived momentum flux. To achieve this, all three (3) criteria must be satisfied. Most of the observed cases which met criterion #4 either lacks criterion #1 or #2. This is to say that most of the cases have similar or the same period in three (3) emission layers and one rotational temperature similar to the work of Nyassor et al. (2018). On the other hand, majority of the events have similar or the same period in just two (2) emission layers.

4.1 GW Event on 04 - 05/12/2004

In Figure 7, that is the 04/12/2004 GW event, the reconstructed GW oscillations (red solid line) using the observed periods determined in the OI, O_2, NaD and OH emission layers overplotted on the residual is presented in panel (a). The dominant periods used in the reconstruction of the waves in GW event #01 are 00.42 h (25.47 min) and 00.50 h (30.29 mins). The wave of $\tau = 25.47 \pm 02.40$ min was observed in all the four emission layers. For the second wave of this event, two similar periods, $\tau = 30.29$ min and $\tau = 33.47$ min were observed. The wave with $\tau = 30.29$ min, was detected in the OI, O_2 and NaD emission layers. However, the observed period in the OH was 0.55 h (33.47 min). Even though this period may differ from the period determined in the other emission layers, its deviation was not out of the error margin of the estimation and thus was considered. The period $\tau = 33.47 \pm 03.16$ min is used in subsequent analysis. The error ranges were within $\pm$ 10% of the estimated periods.

The consideration was based on the fact that this are observed observed periods which were determined under the influence of background wind.

In panel (b), the normalized residual of the reconstructed time series presented for each emission intensity and rotational temperature is shown. The normalization is computed so as to standardize the range of variations in all the emission layers. From the normalized intensity variations, panel (c) was produced, from which the phase differences were determined. From the phase progression, an upward phase propagation, indicated by the first four black vertical dashed lines, was observed. For these four dashed vertical lines, a sharp upward phase propagation (nearly vertical) was observed across the four emission layers of OI, O_2, NaD and OH, between 23:00 UT on 04/12/2004 and 01:30 UT on the 05/12/2004. Between the hours of 01:30 and 02:20 UT on the 05/12/2005, a steep upward phase propagation can be seen between OI, O_2 and NaD emission layers after which a downward phase propagation was then observed between NaD and OH. The turning point of the phase lines of the red dashed lines is highlighted by the light red background, whereas the entire red vertical dashed lines are emphasized by the gray background.

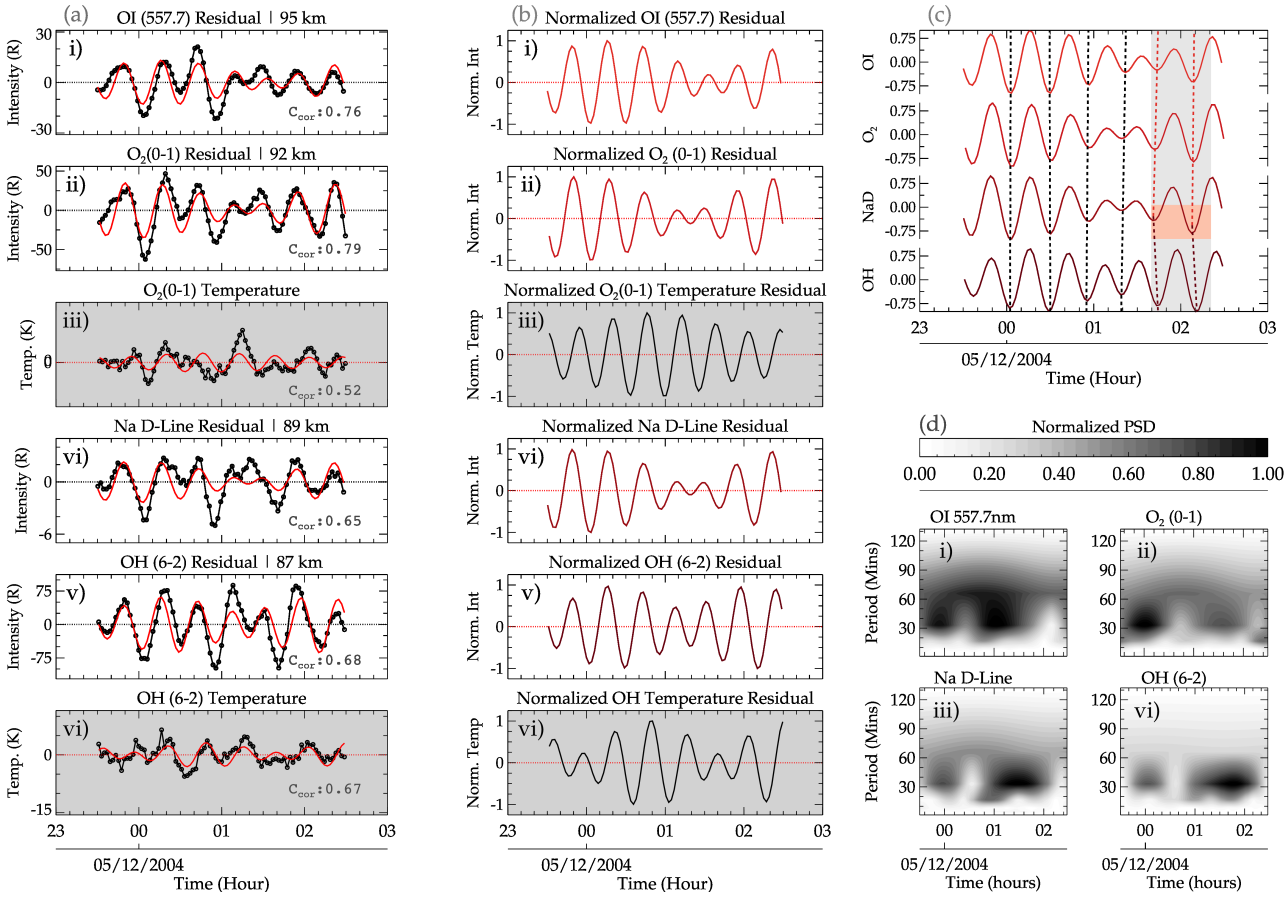

Figure 7. The detailed description of the processing stage of the preprocessed data (obtained form Figure 3). The reconstructed harmonics of the gravity wave oscillations (red solid line) using the dominant periods determined by Wavelet analysis and Lomb-Scargle periodogram, and the residuals for each airglow emission layer and the rotational temperature are presented in panel (a). The corresponding normalized residuals are shown in panel (b). Using the normalized residuals in panel (c), the phase propagation of the gravity wave oscillation at each emission layer altitude is determined using the vertical slanted dotted lines. The gray background emphasizes the red vertical dashed lines whereas the turning point of the phase lines of the red dashed lines are highlighted by the light red background. In panel (d), the Wavelet analysis result of each emission layer is shown.

The observed periods estimated using Wavelet analysis is presented in Figure 7(d). A strong presence of a range of wave periods between 25 mins to 90 mins were observed in all the four (4) emission layers with dominant periods of 25.47±02.40 min (all emission layers), 30.29 min (for OI, O_2 and NaD) and 33.47 min (OH). As mentioned earlier, only the period 33.47±03.16 min is considered in the subsequent analysis. These dominant periods were also present in the Lomb Scargle periodogram as shown in Figure 5. The plots in panel (d) are normalized to standardize the variations of the individual emission layers with the scale defined in the color bar.

Peak selection procedure considering the power spectral densities (PSD) were used to detect the significant periods. It is important to emphasize that GW events with the same periods / similar periods (within $\pm 5\%$ deviations) were chosen. The deviations were included in the choice of periods because they are observed periods which are susceptible to the background wind. Using these periods and Equation 2, the time series (black solid line with open circle) for each emission layer is reconstructed (red solid line) as shown in panel (a) of Figure 7. Unlike Figure 3, the residuals of all the emission layers are plotted, including the rotational temperatures of OH and O_2. Similar to Figures 5 and 6, the rotational temperatures are presented in the plots with gray background in panels (a.iii) and (a.vi) in Figure 7. In panels (b.i) - (b.vi) of Figure 7, the normalized reconstructed residual for each emission layer (including the rotational temperatures of OH and O_2) are presented.

From the reconstructed time series, a similarity can be seen in all the emission layers, which serve as an indication of similar GWs propagating through these layers. Even though similarities exist in the periodicities, some degree of variations can be seen. These variations can be attributed to the variations of the background wind, since the result obtained in the Lomb Scargle periodogram and the Wavelet are observed periods. It is worth mentioning that the time series of the rotational temperature has also been subjected to all the above mentioned procedures to confirm that similar waves observed in the intensity are also present in the temperature. In panel (c), the normalized reconstructed time series intensity is plotted in ascending order of altitude, from which the phase progression of the waves with altitude is determined. Using the dashed vertical lines, the phase progressions are determined.

4.2 GW Event on 01/05/2005

In Figure 8 (which is similar to Figure 7), panels (a), (b), (c) and (d) have the same arrangements. However, this event started at 18:00 UT to 23:30 UT on 1/05/2005. In all subpanels of panel (a), the reconstructed time series (red solid lines) using Equation 2 are plotted with the corresponding residuals of the airglow intensity variations as well as the O_2 and OH rotational temperatures. To assess how best the reconstructed time series fits the residual, the cross correlation (C_{cor}) was estimated and presented in each subpanel of panel (a). In panel (b), the respective normalized intensities and rotational temperatures are presented.

The periods determined in each emission layer using a Wavelet analysis are presented in Figure 8(d). In subpanels (i), (ii), (iii) and (iv) of Figure 8(d), the spectrogram indicating the power spectral densities (PSD) relating the intensity of the periodicities of the wave to the time of occurrence for OI, O_2, NaD, and OH emission layers is presented. The PSD for all the airglow emission layers has been normalized. The scale of the variations is defined by the color bar. A broad spectrum of high PSD of the periods were observed extending from 30 to $\sim$90 min throughout the entire observation window with a peak centered around the early hours of the observation, through the middle and the later time of the observation (especially for the OH emission). The summary of the wave parameters of the photometer observation are presented in Table 3.

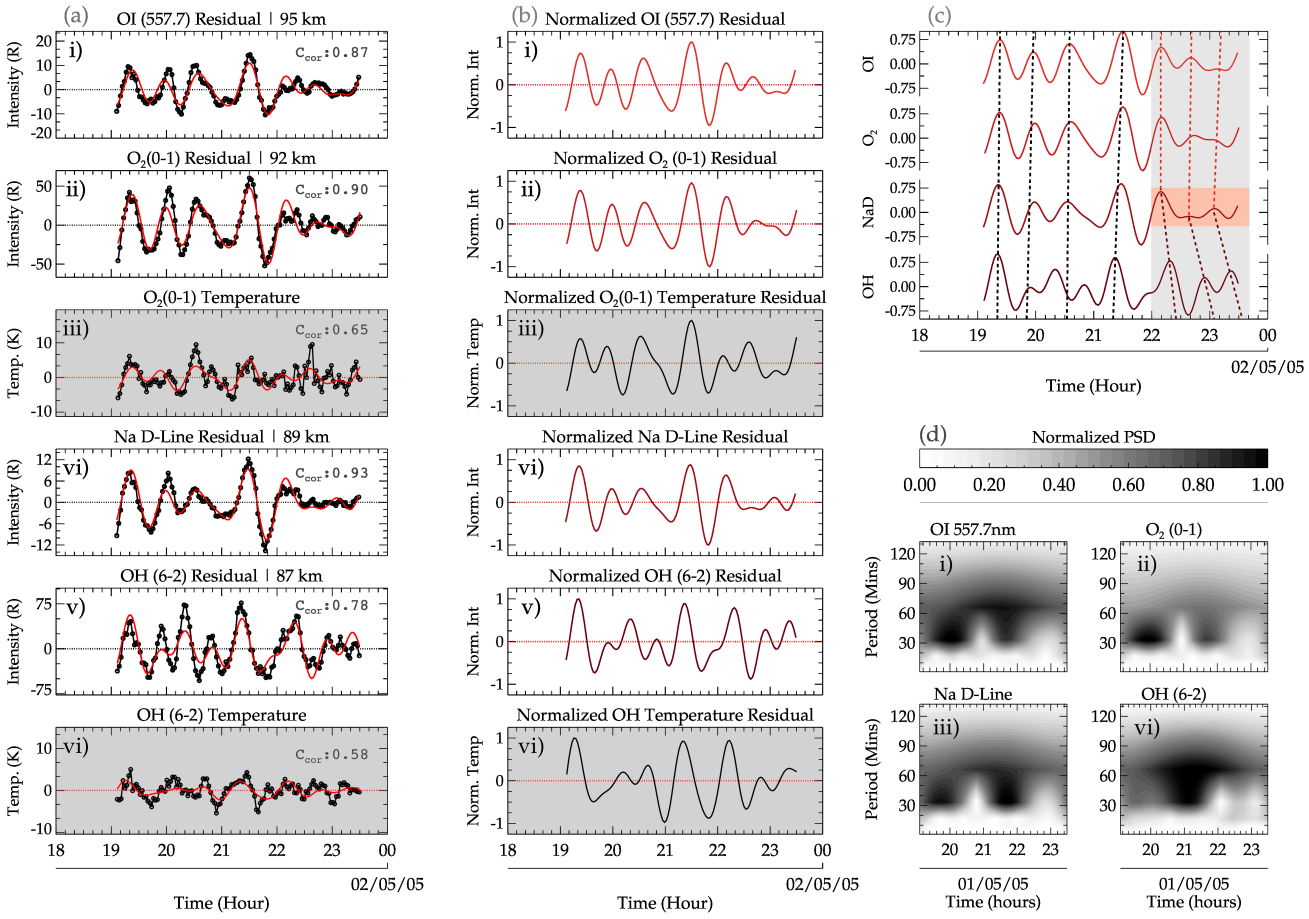

Figure 8. Same as Figure 7 but for 01/05/2005 GW event.

In panel (c) of Figure 8, the phase lines indicating the phase propagation across the four (4) emission layers are presented. Between the hours of 19:30 and ~22:00 UT, a steep upward phase propagation extends from the OH through NaD and O_2 to the OI emission layers. After 22:00 UT till the 23:30 UT, the phase propagation was upward between the emission layers of NaD and OI, whereas between NaD and OH, phase propagation was down.

Table 3. Summary of the selected gravity waves events.

Events	Photometer			All-Sky Imager		Parameters	
	τ_z (min)	V_z (m/s)	λ_z (km)	τ_H(min)	λ_H (km)	M_F (m^2/s^2)	E_p (J/kg)
Event #01							
$\tau_1(O_2)$	25.47 ± 02.40	inf	inf	23.10±1.20	91.00 ±6.30	03.50 × 10^{-5}	44.33
τ_1(OH)						01.24 × 10^{-5}	11.53
$\tau_2(O_2)$	33.47 ± 03.16	05.28 ± 01.25	10.60 ± 02.50	33.60±1.70	135.41 ±11.59	419.50 × 10^{-3}	44.33
τ_2(OH)						07.30 × 10^{-3}	11.53
Event #02							
$\tau_1(O_2)$	31.64 ± 02.93	62.84 ± 11.43	119.31 ± 21.70	28.90±1.40	255.90 ±17.60	13.80 × 10^{-3}	104.62
τ_1(OH)						00.30 × 10^{-3}	7.13
$\tau_2(O_2)$	43.25 ± 04.06	108.08 ± 19.55	280.50 ± 25.38	46.20±2.30	237.00 ±14.40	34.80 × 10^{-3}	104.62
τ_2(OH)						00.90 × 10^{-3}	7.13
$\tau_3(O_2)$	58.43 ± 05.49	11.64 ± 02.17	40.80 ± 07.62	61.03±3.10	454.40 ±26.20	95.40 × 10^{-3}	104.62
τ_3(OH)						01.50 × 10^{-3}	7.13

5 Discussion

5.1 Phase Propagation

As presented in Section 4, two events of similar periods were selected. For Event #01, two dominant periods were detected, however, estimated phase propagation associated with the first period indicates little or no phase change, implying near vertical propagation which is indicative of a possible ducted wave. For Event #02, the three dominant observed periods were determined. In Figure 9, the phase leads and lags between the four emission layers are presented. This figure is intended to determine by how much these GWs with similar periods propagating through the emission layers lag or lead the preceding or succeeding layers using the phase shifts.

5.1.1 Event #01

From the phases of the GWs of Event #01, OH leads NaD by 8.60 min, whereas NaD leads O_2 by 1.21 min. O_2 lags OI by 3.25 min. A consistent phase lead can be observed from OH through NaD to O_2 except between O_2 and OI, where a phase lag was observed. The phase lag observed between the emission layers of O_2 and OI was induced by the background wind due to a shear. From the average wind between 23:30 and 02:30 UT in the direction of the wave, there exist a wind shear between 80 and 98 km as shown in Figure 10(a.iii). This contributed to the phase shift of the waves. From Figure A6, a change in the direction from east to west above the OH emission layer in the zonal wind within the observation hour of the event.

Above the NaD emission layer the zonal wind became predominantly westward and peaks in the O_2. Similarly, the meridional wind also exhibits a change in direction from north to south within the NaD layer during the observation window of the GW event. Despite this phase lag, the mean phase propagation of these GWs shows that OH leads OI by ∼06.58 min. Using this phase information and the period, Figure 9 is produced. These figures are used to evaluate the phases of the GWs in these two emission layers.

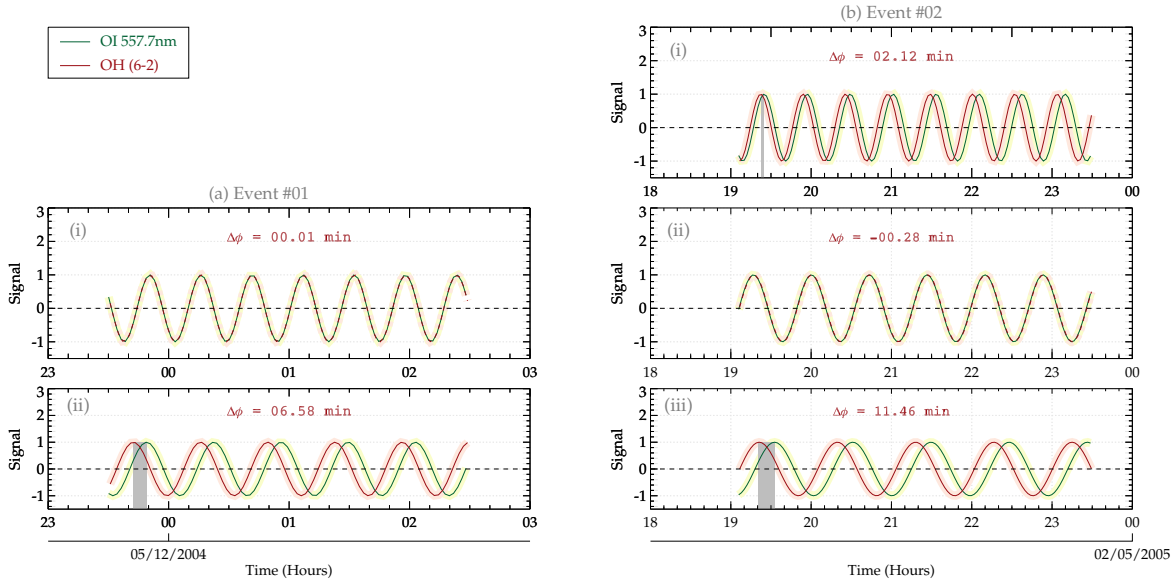

Figure 9. Two observed vertically propagating gravity wave (GW) events at São João do Cariri. In panel (a), the phase difference is determined using the reconstructed signal of O_2 and OH for Event #01. Using the reconstructed signal for each period in Event #02, the phase differences between O_2 and OH are determined and presented in panel (b).

In Figure 9, the reconstructed time series of GW events #01 and #02 are presented. In panel (a), the reconstructed time series of the GW of 04/12/2004 is shown. Subpanels (i) and (ii) show the reconstructed GWs of $\tau_1 = 25.47 \pm 02.40$ min and $\tau_2 = 33.47 \pm 03.16$ min, respectively. Based on the estimated phase difference ($\Delta\phi$) of 00.01 min of τ_1, the vertical velocity (V_z) and wavelength (λ_z) goes to infinity. This indicates very little or no phase difference. For τ_2 of GW event 04 - 05/12/2004, OH leads OI by $\Delta\phi = 06.58$ min. This phase difference led to $V_z = 05.28 \pm 01.25$ m/s and $\lambda_z = 10.60 \pm 02.50$ km. The summary of the estimation $\Delta\phi$, V_z, and λ_z for Events #01 and #02 are presented in Table 3.

5.1.2 Event #02

The phase propagation characteristics of GW event #02 (01/05/2005) is shown in Figure 9(b). The individual reconstructed GWs of each period were constructed using the observation time of the data. In the subsequent subsections, the characteristics of the phases are discussed.

$\tau_z = 31.64$ min

For Event #02 (see Figure 6), propagation of the GW with $\tau = 31.64$ min shows a steep vertical downward phase propagation with altitude. Here, OH leads the NaD by 0.698 min (∼41.890 sec), NaD leads O_2 by 01.926 min, and O_2 lags OI by 00.502 min (∼30.136 sec). In general, OH leads OI by 00.0354 h (02.122 min). In comparison, Figure 9(b.i), a phase lead was observed between OH (red solid line) and OI (green dashed line) emission layers. In Figure 9(b(i)), the phase difference ($\Delta\phi$) between OH and OI is represented by a positive ($+$) value to indicate a lead.

$\tau_z = 43.25$ min

The second period ($\tau_z = 43.25$ min) of Event #02 demonstrated a mixture of phase leads and lags in the phase propagation from OH through NaD and O_2 to OI emission layers, showing a steep vertical upward phase propagation for the first four (4) hours of the time series. No phase difference exists between OH and NaD, whereas NaD was found to lead O_2 by 0.00854 h (∼00.512 min / ∼30.748 sec). In the case of O_2 and OI, O_2 lags behind OI by 00.0132 h (∼00.793 min / ∼47.556 sec). Between OH and OI, OH lags OI by 0.00467 h (∼0.280 min / ∼16.808 sec). The phase propagation characteristics of this GW is shown in subpanel (ii) of Figure 9(b). Here, the $\Delta\phi$ is negative due to the phase lag.

$\tau_z = 58.43$ min

The GW of period, $\tau_z = 58.43$ min, of Event #02 demonstrated a consistent phase lead from OH through NaD and O_2 to OI emission layers, indicating a vertical upward phase propagation between the four emission layers. The GW of this period indicates that OH leads NaD by 0.086 h (∼05.136 min), NaD leads O_2 by 0.0828 h (∼04.970 min) and O_2 leading OI by 0.0225 h (∼01.351 min). Generally, OH leads OI by 00.190 h (∼11.456 min). The phase propagation characteristics using the reconstructed time series of this GW is presented in subpanel (iii) of Figure 9(b). The $\Delta\phi$ is positive due to the phase lead.

GWs phase propagation are used to determine the energy propagation (Nyassor et al., 2018, and references therein). A downward phase propagation indicates upward energy propagation and vice versa. In the case of Event #01, the phase across the four emission layers is upward and almost vertical; thus, the wave energy propagates almost vertically downward for the period ($\tau_1 = 25.47 \pm 02.40$ min). The characteristics of both of these events are similar, except that, one of the periods of the GW in each event (i.e., τ_2 of Event #01 and τ_3 of Event #03) presented a well-defined vertical and upward phase propagation. The remaining period (as mentioned earlier) showed a very steep vertical phase line between the emission layers due to the little or no phase difference, which causes V_z and λ_z to approach infinity (presented in Table 3).

The downward phase propagation indicates that this wave is generated upward and propagates downward (Vadas et al., 2018). Downward propagating GWs, just like upward propagating waves, transport momentum and energy from the source location, thus depositing this momenta and energies wherever they break or dissipate. However, these two cases presented three different dynamics:

1. almost vertical phase propagation across all emission layers;

2. an upward and downward phase propagation (fish bone structure) at the later hours of the observation times and;

3. out of phase variation of the O_2 and OH rotational temperatures at the later hours of the observation time.

These dynamics are discussed in detail together with the propagation conditions of the GWs across these emission layers as well as the characteristics of the momentum flux and potential energy.

5.2 Background Propagation Conditions

Due to the characteristics of the phase propagation of the two events considered in this study, the propagation conditions between 80 and 100 km were investigated. Figure 10 (a) and (b) represent the propagation conditions of GW events #01 and #02, respectively. In panels (a(i)) and (b(i)), the temperature profile obtained from SABER observation (solid line) and the estimated potential temperature (dashed lines) are presented. The potential temperature (θ) was estimated using Equation 6. The profile of the Brunt Väisäla frequency (N) presented in panels (a(ii) and (b(ii)) was estimated using Equation 5. The Brunt Väisäla frequency profile is mostly used to examine the formation of duct called thermal duct due to temperature gradient (Bageston et al., 2011). Ducts are known to trap vertical propagating GWs, causing them to propagate horizontally for longer distances and time.

Doppler duct, on the other hand, are caused by background wind gradient (Bageston et al., 2011; Isler et al., 1997). To determine whether or not the propagation of GWs are hindered or favored by the background conditions (controlled mainly by wind and temperature), the square of the vertical wavenumber (m^2) profile is used. The m^2 can be estimated using (Bageston et al., 2011):

$$m^2 = \left[\frac{N^2}{(u_0 - c_H)^2} - \frac{u_o''}{u_0 - c_H} - k_H^2\right], \tag{10}$$

where, N is the Brunt Väisäla frequency, u_0 is the observed horizontal wind in the direction of the wave propagation, u_o'' is the second derivative of the wind with altitude, c_H is the observed horizontal phase speed, $k_H = 2\pi/\lambda_H$ is the horizontal wavenumber with λ_H being the horizontal wavelength. Equation 10 is a valid dispersion relation for gravity waves propagating in an environment where the effects of horizontal wind and temperature gradient cannot be neglected (Chimonas and Hines, 1986).

The profile of the horizontal wind in the direction of the wave propagation, $u_o = u\cos\psi + v\sin\psi$, is shown in panels (a(iii)) and (b(iii)) of Figure 10. Here, u and v are the zonal and meridional wind components, respectively, and ϕ is the propagation direction of the GW observed in the all-sky images. Using the other parameters defined in Equation 10, the m^2 profile is estimated and plotted in panel (a(iv)) and (b(iv)).

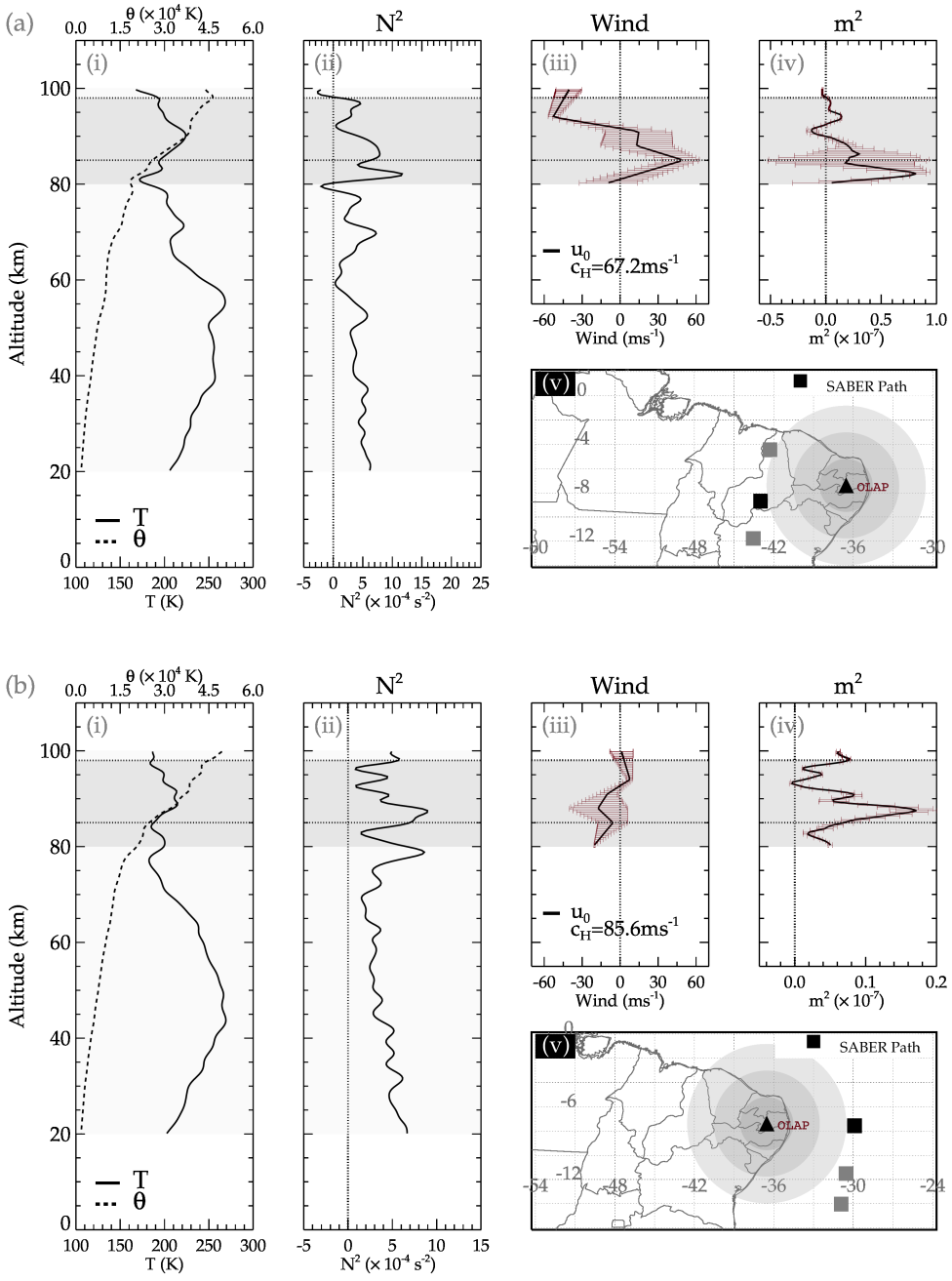

Figure 10. Propagation characteristics of the GW events observed on the 04 - 05/12/2004 (panel (a)) and 01 - 02/05/2005 (panel (b)) GW events. Kinetic temperature profile in (i) of the selected SABER soundings position of the profile is shown as black square in (v). The dashed line in (i) is the profile of the potential temperature. In (ii) the profile of Brunt Väisäla frequency is presented. In panels (iii) and (iv), the profile of the wind in the direction of the GW propagation and the m^2 are presented, respectively.

In panels (a(v)) and (b(v)), the geographical map of the OLAP facility and the sounding positions of the SABER satellite are presented. The positions of the SABER sounding indicated by the squares, among which the temperature profile of the black square is selected to compute the potential temperature and the Brunt Väisäla frequency. The sounding positions during Event #01 started from -43.54°, -11.77° occurred at 00:47:29 UT through -43.00°, 08.70° at 00:48:30 UT to -42.28°, -04.45° at 00:49:41 UT. For Event #02, the sounding position started from -29.90°, -07.56° at 18:46:35 UT through -30.54°, -11.51° at 18:45:24 UT to -30.90°, -14.04° at 18:44:39 UT. These sounding positions and times fall within a defined radius of 800 km around the observation site. This radius was defined so that any sounding that fell within would be considered.

Several studies have demonstrated how the background conditions control the propagation characteristics of GWs. Using the m^2, the evanescent ($m^2 < 0$) and propagating ($m^2 > 0$) regions can be determined. Most ducts are formed when two evanescent regions exist above and below a region of $m^2 > 0$. From Figure 10, panels (a(iv)) and (b(iv)), show the profiles of m^2 estimated using observed parameters. As mentioned earlier, ducts are formed when there is a gradient in the background temperature and wind. In both cases, a gradient can be observed in the temperature and wind (see the gray shaded region in panels (i) and (ii)), indicating a possibility of a duct formation.

The m^2 profile, however showed structures of existence of a duct. During the GW event #01, two ducted regions can be observed; the first one between ∼91 and 98 km and ∼80 and 90 km. The first duct encloses most likely the the peak altitudes of O_2 and OI emission layers. Even though this duct may appear quite weak, it is possible that had contributed to the trapping of the GW within this emission layer. The second duct, which is stronger than the first, most likely favored the trapping of the GWs in the peak altitudes of OH and NaD emission layers. Despite the presence of the structure of duct, the GW phase propagation presented a characteristic that appeared to be an effect of a single duct. This is because, except a slight difference in the observed period of the τ_2 GWs of event #01 in the OH emission, all other emissions have the same period.

For the event #02, the structure of the duct presented almost the same characteristics as Event #01. An inversion layer could be observed in the temperature profile as shown in panel (b(i)). However, this inversion layer did not significantly influence the formation of the duct as shown in Figure 10(b(ii)). Only one observed evanescent region was formed at ∼94 km. Around 83 km, a lower evanescent region can be seen forming despite not attaining $m^2 < 0$. Even though the m^2 profile had a structure of a duct, only one evanescent region was formed. Besides this, the characteristics of the GWs observed in this event are similar to that of event #01. Considering the propagation dynamics of this wave, which is suggestive of the influence of ducts, it is most probable that this structure might play an important role in the dynamics of the vertical propagation of this event.

5.3 Assessing the Duct Formation and Contributing Factors

Formation of duct and its dynamics are mainly controlled by wind and temperature. These parameters are defined in Equation 10: (1) the buoyancy term, $N^2/(u_0 - c_H)^2$, resulting from the temperature and (2) the curvature, $u''/(u_0 - c_H)$, term due to wind. To do this assessment, either the buoyancy term or the curvature term is ignored in Equation 10. Neglecting the curvature term, Figure 11(a(i)), a broad duct extending from ∼80 km to 98 km is formed, with a maximum m^2 of $\sim 0.85 \times 10^{-7} \mathrm{m}^2$. However, the lower part of the evanescent region is not well formed and this can be attributed to the limitation of the wind data to 80 km. Below 93 km the duct broadens to the lower (quasi) evanescent region extending down to 80 km. For event #01 and

considering only the curvature term (see Figure 11(a(ii))), two weak ducts were formed centered around 85 and 92 km with a maximum m^2 of 0.5×10^{-7}m^2 and 0.2×10^{-7}m^2, respectively.

The assessment for Event #02 is presented in Figure 11(b). In the case where the curvature term was ignored (considering only buoyancy term), a duct with two maxima were formed between ∼80 and 93 km with a peak of $\sim0.16\times10^{-7}$m^2. Above ∼93 km, a narrow peak was also formed. Similar to the buoyancy term of Event #01, the lower limit of the evanescent region of this duct was not completely formed. Now, ignoring the buoyancy term as shown in Figure 11(a(ii)), the peak magnitude of the duct due to the curvature term is 0.04×10^{-7}m^2 (see panel (b(ii))). Two weak ducts were formed with peaks around 85 and ∼93 km, with a broad evanescent region extending from ∼87 to ∼92 km.

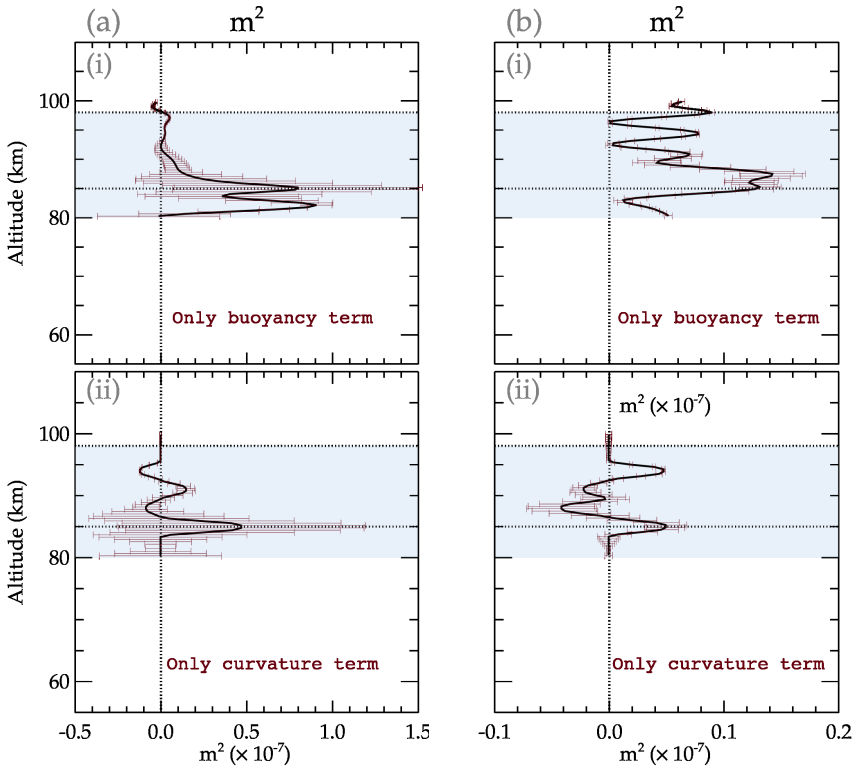

Figure 11. Assessing the influence of the buoyancy and curvature terms on the propagation characteristics of the GW events observed on the 04 – 05/12/2004 (panel (a)) and 01 - 02/05/2005 (panel (b)) GW events.

From Figures 5 and 11, it can be observed that there is a possibility of existence of ducts. These ducts are mainly due to temperature gradients. However, the ducts are considered weak (due to low m^2 values) and also having multiple ducts with some not having a well formed evanescent region ($m^2 < 0$). The observed ducts in this work can be said not to give the entire structural dynamics because the sounding positions during the GW events were quite distant from the observation site. From the phase lines, little or no phase differences were observed during the first two hours of Event #01 and approximately the first three hours of Event #02. Using the phase difference, except for a period in each event, the estimated vertical wavelength (λ_z)

approaches infinity thus vertical wavenumber ($m \to 0$). This characteristic causes the wave to undergo total internal reflection (Gossard and Hooke, 1975). Due to the limitation of the photometer airglow observations, the full extent of the dynamics cannot be explored. This will be explored in a future paper.

5.4 Fish borne Structure and Out-of-Phase Temperature Variation

Figures 5 and 6, show an upward and a downward phase progression, forming a fish borne structure (as described in the work of Vadas et al. (2018)). In their work, the authors applied a procedure to explore whether or not the turning points in both cases (which occurred around the NaD emission layer) were a reflection point or a region where dissipation occurred and whether these possibly led to the excitation of other spectrum of GWs. It is known that for GWs to be considered as non-primary waves as shown by various works (e.g, Vadas et al., 2003, 2018; Kogure et al., 2020; Heale et al., 2020), the GW propagation characteristics for the upward and downward components must meet certain criteria defined in Vadas et al. (2018). However, these criteria cannot be applied in this study due to limited altitude range. Also, the events considered in this work presents GWs with similar or nearly the same periods propagating through the NaD, O_2, and OI emission layers except for OH which differs slightly but fell within the error margin. This shift in the period (see Figures 5(a and b)) could be due to the wind in the GW propagation direction.

Despite no existing evidence in the m^2 profile to explain the fish borne structure, the rotational temperature variation of the OH showed a shift and eventually got out of phase with the O_2 rotational temperature and the remaining emission layers (see Figure 4). This characteristic had been reported by Takahashi et al. (1998, and references therein) to be due to reflected GWs. Therefore, considering the fact that the OH rotational temperature is out of phase with O_2 rotational temperature and the remaining emission intensity variation at the later times of the observation or usable window of the data considered in this, the possibility of a reflection is indicated.

6 Momentum Flux and GW Potential Energy

Gravity waves transport momentum and energy from their excitation/source location to their sink (dissipation/breaking), whether the waves are upward or downward propagating (Fritts and Alexander, 2003; Vadas et al., 2009; Nyassor et al., 2021). The amplitude of upward propagating GWs grows due to the decreasing density with increasing altitude. So, for a downward propagating wave, the amplitude of the wave may suffer amplitude decrease due to increasing density with decreasing altitude. In Section 5.1, two GW events are selected with an upward phase propagation. The phases analyzed in Figure 6 further showed phase leads and also small phase shifts. The individual reconstructed signal using the wave phases and periods affirms there exist phase differences between OI and OH emission layers.

According to Vadas (2007), diffusion processes inhibit the propagation of GWs where molecular viscosity and thermal diffusivity are significant in the upper mesosphere and lower thermosphere. Turbulent diffusion is also known as a significant process that inhibits gravity wave propagation in the lower and middle atmosphere (Yiğit and Medvedev, 2016). However, high-frequency GWs with relatively large intrinsic horizontal phase speeds mostly survive these conditions and are capable

of directly propagating to the upper atmosphere, where they break or dissipate Yiğit et al. (2021). However, what will be the characteristics of GWs momentum flux and potential energy for either an upward or downward propagating gravity wave, when they happen to be in a duct? These features are evaluated from the momentum flux and potential energy of the GWs derived from the rotational temperatures of the O_2 and OH emission layers.

6.1 GW Event #01

The momentum and potential energy variation with time (and averages) at the O_2 and OH emissions are presented in Figure 12 for the GW event of 04/12/2004 (event #01). Note that the same/similar period GWs determined in the variation of intensity of the four emission layers were determined in the rotational temperatures of the O_2 and OH. In Figure 12(a, b, c, d), background temperature, residual, potential temperature and Brunt Väisäla frequency time series are presented.

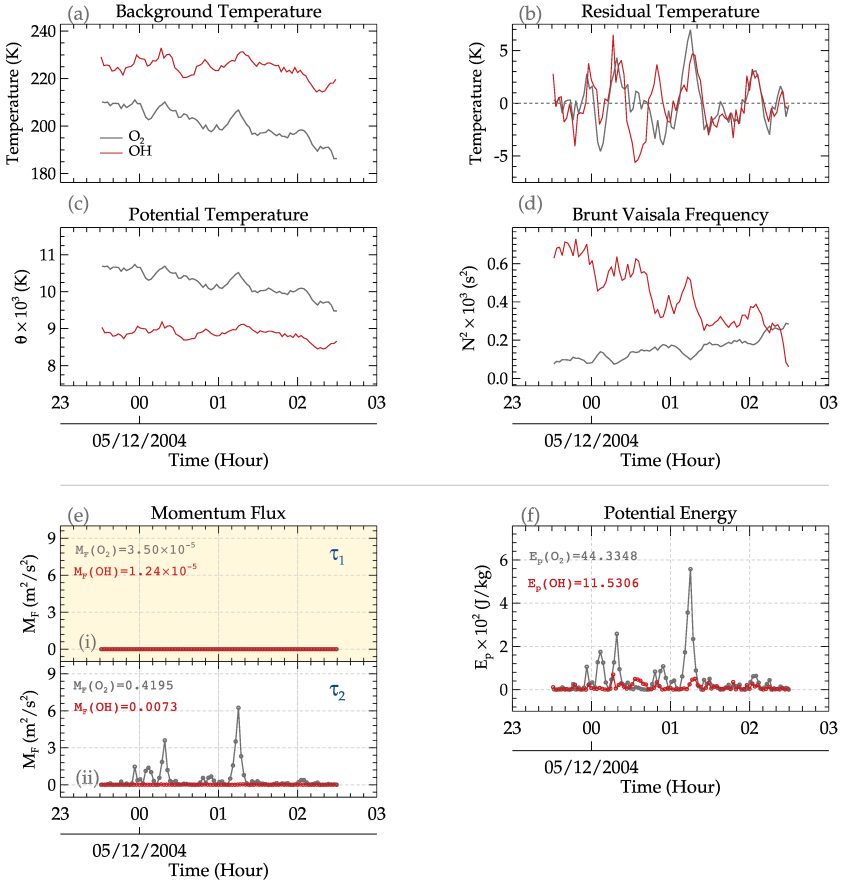

Figure 12. The characteristics of momentum flux (e) and potential energy (f) at the O_2 and OH emission altitudes for the event of 04/12/2004. In subpanels (i) and (ii) of panel (e), the GW momentum flux for first and second period of event #01 are presented. The light yellow background (in (i)) highlights the period with steep vertical phase propagation. In panels (a), (b), (c), (d)), background temperature, residual temperature, potential temperature and Brunt Väisäla frequency time series are presented, respectively.

The black solid lines represent the time series of the O_2, whereas the red line indicate the OH time series. The estimated momentum flux at the peak altitudes of O_2 ($\sim$92 km) emission layer and OH ($\sim$87 km) emission layers is shown in panel (e). The momentum flux of each period (labeled $\tau_1 = 25.47$ min and $\tau_2 = 33.47$ min) of the GW in event #01 are presented in subpanels (i) and (ii) of panel (e). Subpanel (i) with the light yellow background highlights the period with the steep vertical phase propagation. The time averages of the momentum fluxes for O_2 and OH indicate that the momentum flux of the GW in the O_2 ($M_{F(O_2)}$) is greater than the momentum flux in the OH emission layer ($M_{F(OH)}$) for τ_2. However, for τ_1, the momentum flux in both emission are approximately zero ($M_F(O_2) \sim M_F(OH) \sim 0$). The potential energy (E_p), on the other hand, in O_2 is higher compared to that of OH.

6.2 GW Event #02

Similar to Event #01, the background temperature, residual temperature, potential temperature and Brunt Väisäla frequency time series are presented in panels (a), (b), (c) and (d) of Figure 13. The momentum flux and potential energy at each emission layer for the three GWs observed in the event of 01/05/2005 is presented in panels (e) and (f). The momentum flux of three periods (labeled $\tau_1 = 31.64$ min, $\tau_2 = 43.25$ min and $\tau_3 = 58.43$ min) of the GW in event #02 are presented in subpanels (i), (ii) and (iii) of panel (e). The periods with near steep vertical phase propagation are (i.e., τ_1 and τ_2) are shown in subpanels (i) and (ii) with light yellow background. The time averages of the momentum fluxes for O_2 and OH indicate that the momentum flux of the GW in the O_2 ($M_{F(O_2)}$) is greater than the momentum flux in the OH emission layer ($M_{F(OH)}$) for all the three periods determined in this event. It is observed that the amplitude of the momentum fluxes for each emission layer increases with the periods (thus, $M_{F_{\tau_1}} < M_{F_{\tau_2}} < M_{F_{\tau_3}}$).

Comparison between the momentum fluxes at O_2 and OH emission layers for this event showed a vast difference in the momentum fluxes. The M_F at the O_2 is much higher than at OH. This difference can be attributed to the large amplitude of the gravity wave perturbations in the O_2 temperature residual since the estimation of the potential energy and the momentum flux depend on the temperature residual. However, for the GW event of 04 - 05/12/2004, the amplitude of the temperature perturbations due to GWs are similar. What made the momentum flux greater in the O_2 altitude are the spikes. Besides these spikes, the momentum flux at the O_2 and OH altitudes are similar. Another explanation for this difference apart from the increase in amplitude due to a decrease in density with altitude, is N^2. The times series of the N^2 varied considerably over the observation window, especially in the OH emission layer for both events.

Comparison between the two events showed that regardless of the vertical propagation of GWs, momentum and energy are transported from the source to the sink. It is imperative to say that the momentum and energy at the source will be less. This has clearly been demonstrated in these two selected events, attesting to the fact that atmospheric density significantly impacts the amplitude, momentum, and energy. Using Lidar temperature profile, Kaifler et al. (2017) studied the dynamics of downward propagating gravity waves. They observed that one third of the momentum flux is carried by the downward propagating GW from 85 km altitude to a lower altitude. In this work, this characteristic could not be accounted for due to the presence of ducts which could possibly change the dynamics of momentum and energy transportation. In general, the momentum flux and potential temperature for both events are higher in the O_2 emission layer than that of OH. It can be postulated that if indeed a

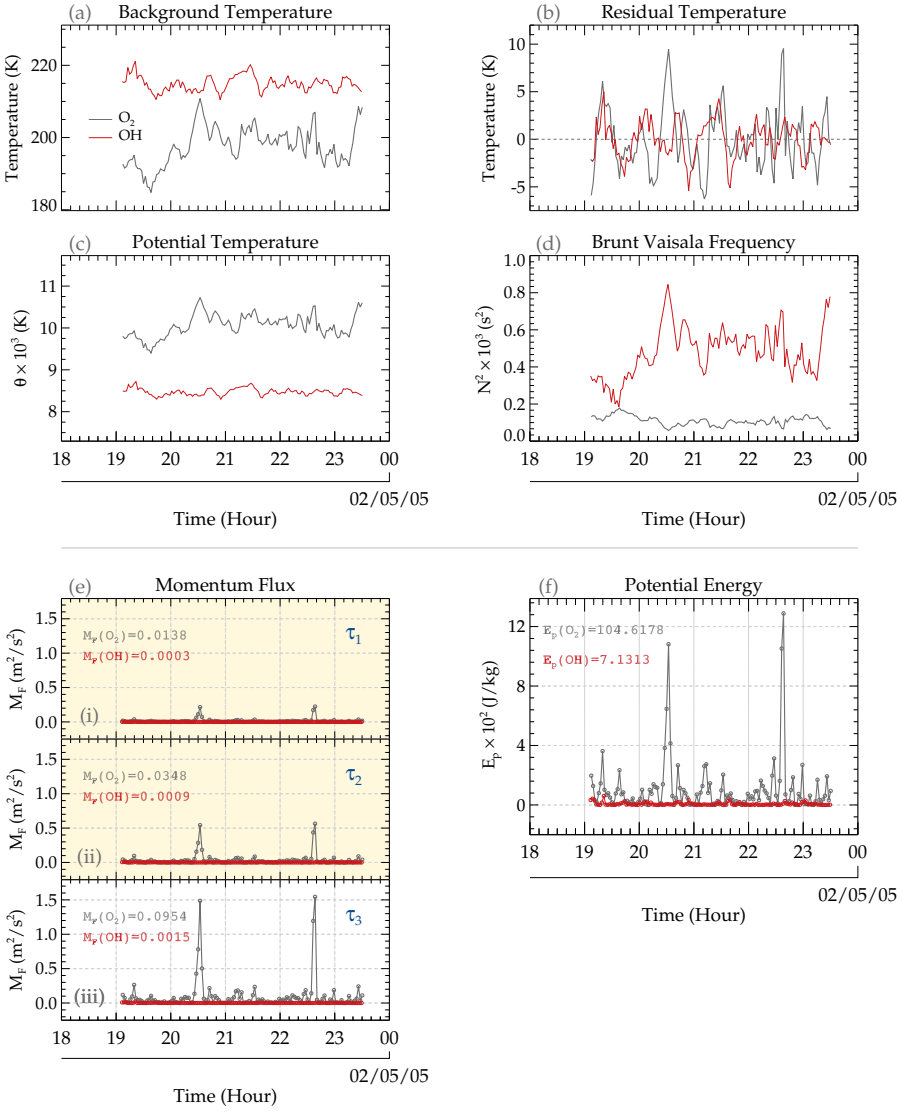

Figure 13. The characteristics of momentum flux (e) and potential energy (f) at the O_2 and OH emission altitudes for the event of 01/05/2005. In subpanels (i), (ii) and (iii) of panel (e), the GW momentum fluxes for first, second and third periods of event #02 are presented. The light yellow background (in (i) and (ii)) highlights the periods with steep vertical phase propagation. In panels (a), (b), (c), (d)), background temperature, residual temperature, potential temperature and Brunt Väisäla frequency time series are presented, respectively.

595 duct exists in each event, then the momentum and potential energy should be higher in the peak region of the duct, where O_2 is situated. At the reflection points (where $m^2 < 0$), the momentum flux and the potential energy should be less. This postulate could not be explored due to lack of high resolution vertical observations between 80 - 100 km. This subject is however intended to be examined in a future paper.

The momentum fluxes of the GWs of periods, that is, τ_1 of event #01 and τ_1 and τ_2 of event #02 with steep vertical propagations presented a different characteristics. As mentioned earlier, the estimated momentum flux of τ_1 of event #01 in both emission layers are near zero (0) indicating no exchange of momentum between the two layers. The near zero momentum flux corresponds to the τ_1, which has steep vertical phase propagation. The phase propagation of the GW with this period is almost the same for each emission, which caused the V_z and λ_z to approach infinity. For event #02 τ_1 and τ_2, even though the momentum flux in the O_2 emission layer is higher than that of the OH layer, the values are lower compared to τ_3. Their phase propagation are near vertical, however, not as in the case of τ_1 of event #01.

Considering the fact that the vertical propagation of these GWs are only within a 5 km range, the full extent of the characteristics cannot be explored due to the unavailability of dataset. The potential energy of Event #01 also depicted characteristics similar to the momentum flux. Lesser momentum flux and potential energy on the OH emission layer is indicative of no deposition of momentum and energy, whereas higher in the O_2 is a pointer to deposition. Thus, it illustrates the governing theory of the transport of momentum and energy by atmospheric GWs. Using a longer altitude range and high temporal resolution lidar data, for instance, this subject can be explored in detail and standards can be defined to determine the signatures of vertical propagating GWs due to reflection and non-primary GWs. In summary, this study has illustrated the possible consequences of ducts on the vertical propagation of GWs and their dynamics (specifically, momentum and energy transportation).

7 Conclusions

This paper studies the dynamic characteristics of momentum flux and potential energy of vertical (almost downward) propagating GWs using two GW events selected for case studies. Using the phase propagation of GWs with almost the same periods through the emission layers of OI 5577, O_2, NaD, and OH, the vertical propagation of the waves was determined. Using the ratio of the altitude difference (Δd) to the phase difference ($\Delta\phi$), the vertical phase speed and, consequently, the vertical wavelength were estimated. From the phase propagation, two classical events each having almost downward propagating GWs were selected for further studies.

The potential energy and momentum flux were estimated, and their characteristics studied. For each propagating GWs, it was determined that the momentum flux and potential energy at the O_2 emission altitudes were higher than those at OH emission altitudes. The momentum flux and the potential energy at the OH emission altitude were far lower than that of the momentum flux at the O_2 emission layer. No distinct amplitude enhancement of GWs were observed in the O_2 as compared to GWs observed in the OH emission layer. The similar GW amplitude of propagating wave in the O_2 and OH rotational temperature indicates a restricted or bounded propagation condition.

Due to the steep phase difference between the four emission layers, background propagation conditions are investigated. The m^2 profile suggested the presence of ducts during the two events. These ducts were found to be created due to temperature inversion. There is no idea about the full extent and dynamics of the ducts because the SABER sounding positions from which the temperature profile were computed are distant from the observation sites. However, $m \to 0$ caused by steep phase line,

suggests total reflection, indicating the presence of ducts. The presence of the duct is further confirmed by the no amplitude difference between the two emission layers.

It was observed that getting to the end of the observation/time series, the OH rotational temperature was out-of-phase with respect the intensity variations of OI, O_2, NaD and OH as well as O_2 rotational temperature. This characteristic is caused by reflection of GW. The observed duct could not be used to support and explain why the OH rotational temperature was out-of-phase. The fish borne structure formed at the end of the observation time typically is suggestive of a reflection since GW with similar periods propagated across.

As mentioned earlier in this work, the altitudinal difference between the two rotational temperatures, is limited to only 5 km, that is, only in the mesopause region. Hence, to come to a definite conclusion whether or not the steep phase lines, high λ_z and the same/similar GW amplitude (residual temperature) are due to the imposing propagation restriction by the duct, a detailed study is intended to be conducted using co-located observations of higher spatial (vertical) resolution. However, this work demonstrated that momentum and energy deposition are affected in the presence of a duct. This characteristic can aid in the setting of boundary conditions when considering the vertical propagation dynamics of GWs.

Appendix A: Retrieval of Gravity Wave Parameters from OH all-sky Images and Meteor Radar Wind Dynamics.

A1 Spectral and Keogram Analysis

In order to extract the parameters of gravity waves, a discrete Fourier transform based spectral analysis was used. First, a region containing GW oscillations were selected in both zonal and meridional component of the keogram components, as shown in Figure A1. Note that the same area in each of the components were considered for analysis. Next, a discrete Fourier transform (Equation A1) is applied to the selected areas (Wrasse et al., 2007; Figueiredo et al., 2018).

$$F(\omega) = \sum_{n-0}^{N-1} f(t) e^{\frac{-2\pi\omega n_i}{N}} \tag{A1}$$

in which $F(\omega)$ is the transform of the Fourier function $f(t), \omega = 0, ..., N-1$ is the frequency index, and N is the number of points in the time series within the selected regions. Then, the cross spectrum defined by

$$C(x) = F_s(\omega) F^*_{s+1}(\omega) \tag{A2}$$

in which $C(\omega)$ is the cross spectrum between two time series and $F_s(\omega)$ and $F^*_{s+1}(\omega)$ represent the Fourier transform of the series $f_S(t)$ and $f_{s+1}(t)$, respectively. $F^*_{s+1}(\omega)$ is the complex conjugate of $F_{s+1}(\omega)$. The one-dimensional cross power spectrum is defined by the quadratic modulus, $|C2|$. The amplitude of the cross power spectrum is then determined using $2\sqrt{|C^2|}$, with the phase of the cross spectrum defined by

$$\Delta\psi = tan^{-1}\left\{\frac{Im(C(\omega))}{Re(C(\omega))}\right\}, -\pi \leq \psi \geq \pi. \tag{A3}$$

The phase difference between these time series caused by the wave propagation is considered to be the frequency ω, corresponding to the maximum amplitude. From the above estimations, the wave parameters are determined as follows:

1. Period (min):

$$\tau = \frac{1}{|f(\omega)|}; \tag{A4}$$

2. Horizontal wavelength (km):

$$\lambda_H = \frac{\lambda_{NS}\lambda_{EW}}{\sqrt{\lambda_{NS} + \lambda_{EW}}}, \tag{A5}$$

where, wavelength (in km) for the zonal and meridional components $(\lambda_{NS}, \lambda_{EW})$ is $\lambda_{NS,EW} = \frac{\Delta d}{\Delta\psi/360^\circ}$, in which Δd is the distance between the time series.

3. The horizontal phase velocity $c_H(m/s)$, and phase propagation direction $\phi(^\circ)$, are determined by

$$c_H = \frac{\lambda_H}{\tau} \quad \text{and} \quad \phi = cos^{-1}\left(\frac{\lambda_H}{\lambda_{NS}}\right). \tag{A6}$$

Five GWs were detected from these two events using the above described spectral analysis. These results are presented below.

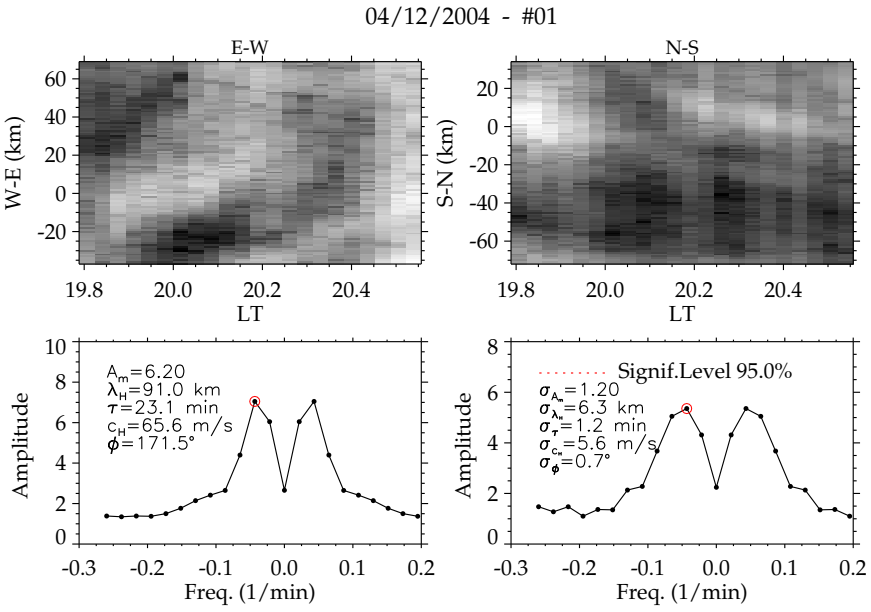

Figure A1. Result of OH emission layer keogram/spectral analysis of Event #01 with period, $\tau = 23.10 \pm 01.20$ min.

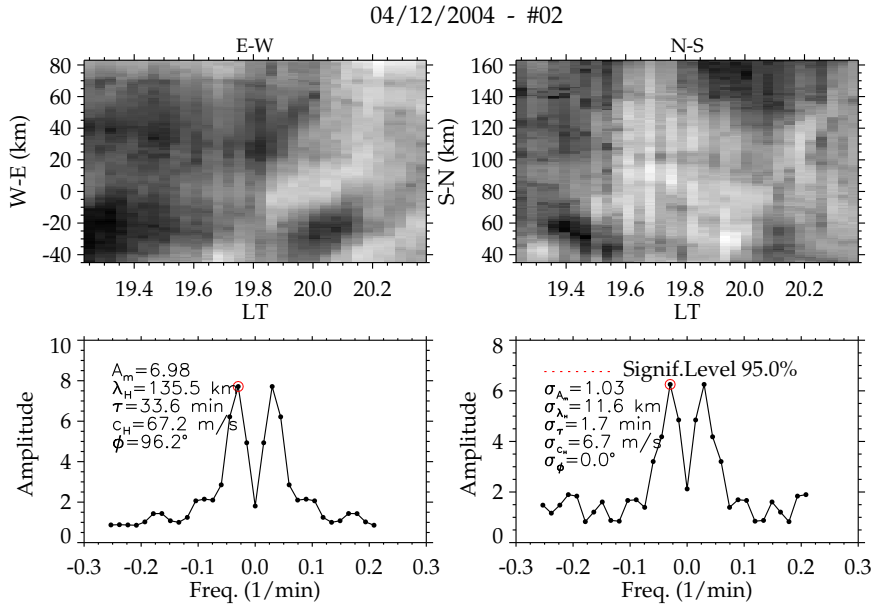

Figure A2. Result of OH emission layer keogram/spectral analysis of Event #01 with period of $\tau = 33.60 \pm 01.70$ min.

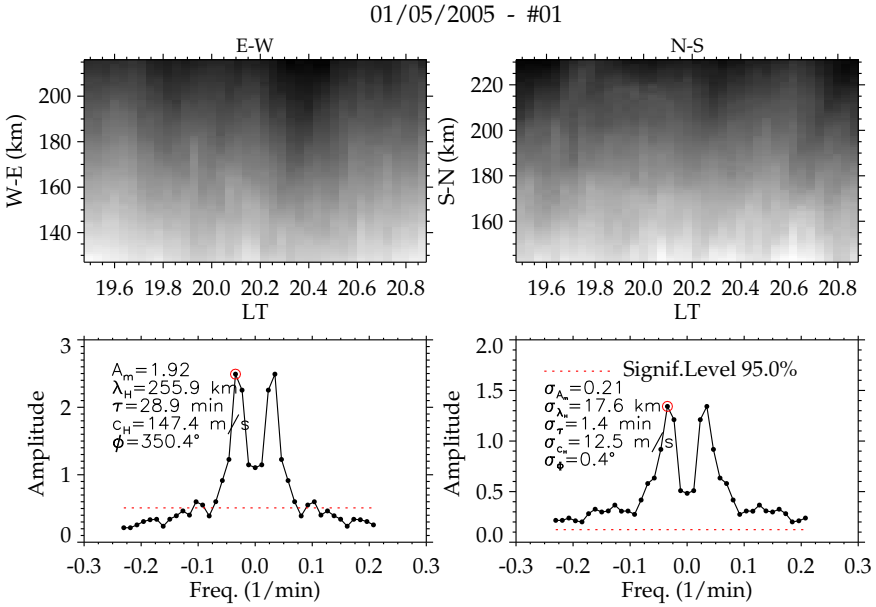

Figure A3. Result of OH emission layer keogram/spectral analysis of Event #02 with period of $\tau = 28.90 \pm 01.40$ min

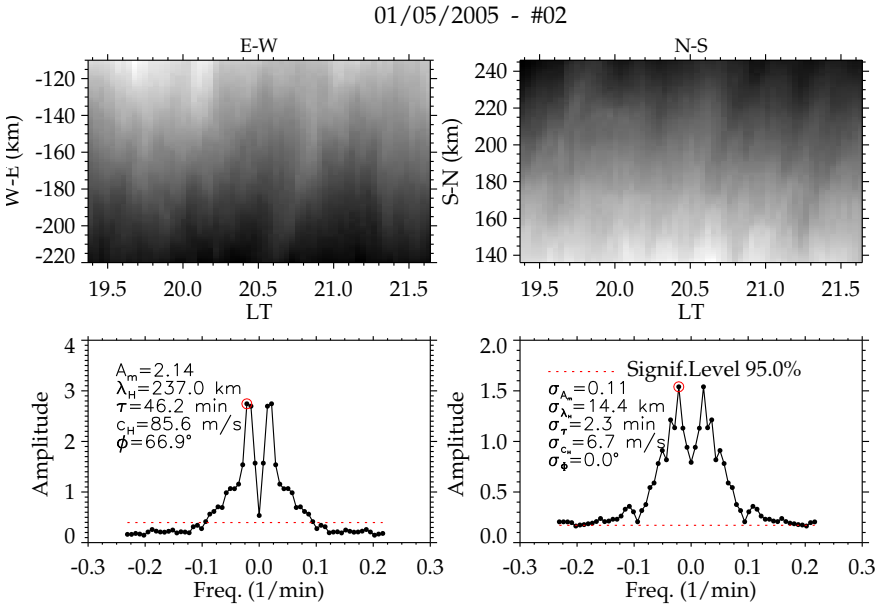

Figure A4. Result of OH emission layer keogram/spectral analysis of Event #02 with period of $\tau = 46.20 \pm 02.30$ min

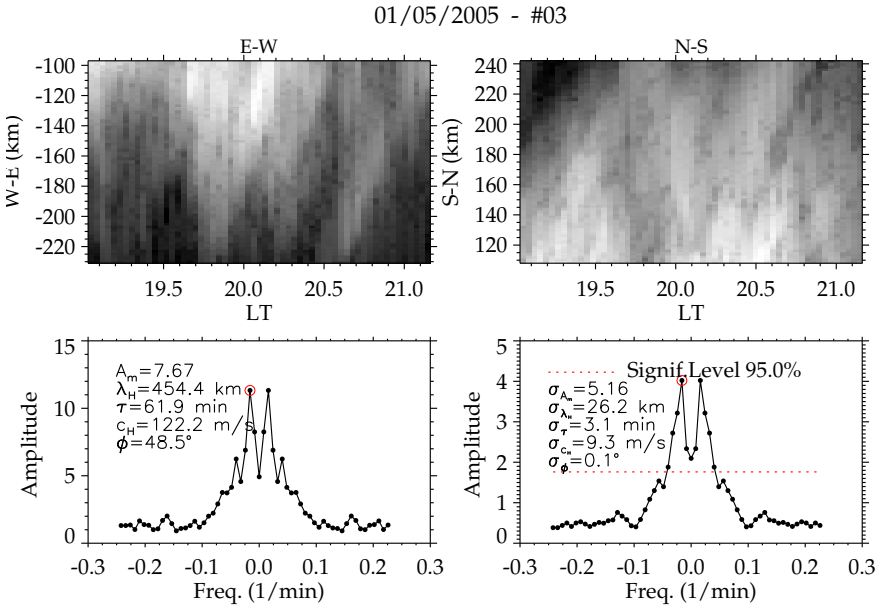

Figure A5. Result of OH emission layer keogram/spectral analysis of Event #02 with period of $\tau = 61.90 \pm 03.10$ min

In the upper panel, (the left side) is the zonal keogram, whereas the right side is the meridional (merid) keogram. These keograms correspond to the selected region with GW perturbations. The lower panel is the amplitude (left) with the GW

parameters listed and their corresponding standard deviation (σ) in the lower right panel. The red dotted horizontal lines indicate a significant level greater than 95.0%, whereas the red circle with a black dot shows the peak amplitude. The GW characteristics in the lower panel are the horizontal parameters (i.e., the sum of the zonal and meridional components).

A2 Observed horizontal wind during the gravity wave events

In Figure A6 and A7, the zonal and meridional winds are presented in panels (a) and (b) are presented.

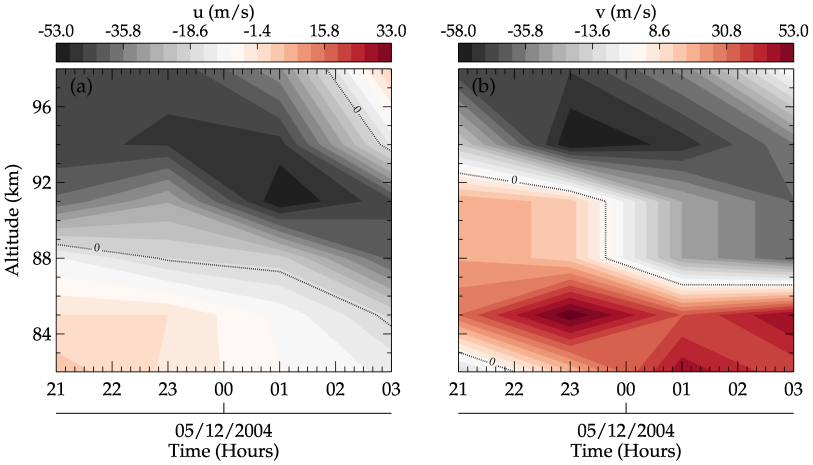

Figure A6. Meteor radar winds during the 04/12/2004 gravity wave (GW) event at São João do Cariri. The zonal and meridional winds are presented in the panels (a) and (b).

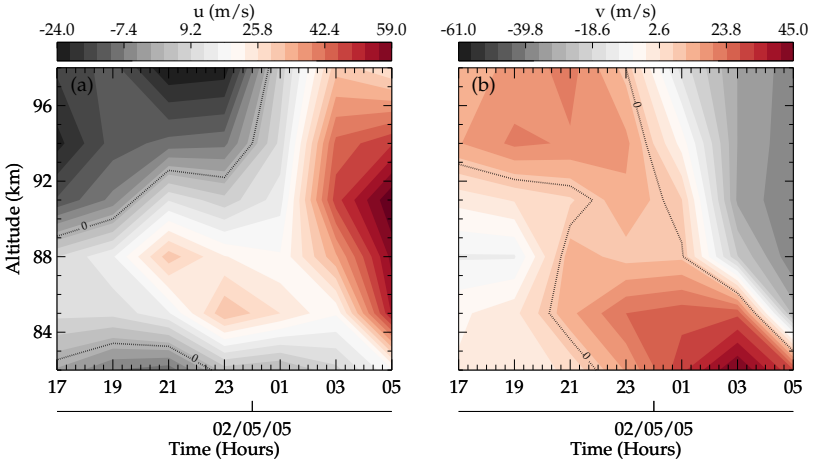

Figure A7. Same as Figure A6 but for the 01/05/2005 gravity wave (GW) event at São João do Cariri.

Author contributions. PKN wrote the article and performed most of the analysis. CMW assisted in the validation of the methodologies and in the revision of the manuscript. IP assisted in the validation of the some methodologies and in the revision of the manuscript. EY assisted in the validation of the methodology and revision of the manuscript. VYTB assisted in the development of some methodologies and revision of the manuscript. RAB provided the photometer and meteor radar data as well as revision of the manuscript. CAOBF assisted in the validation of some of the methodologies and the revision of the manuscript. GAG helped in the validation of some of the methodologies and the revision of the manuscript. FE processed the meteor radar wind data and revised the manuscript. OMA, HT and DG revised the manuscript.

Competing interests. The contact author has declared that none of the authors has any competing interests.

Acknowledgements. Prosper K. Nyassor acknowledge the support of Fundação de Amparo à Pesquisa do Estado de São Paulo (FAPESP). The authors also thank the Coordenação de Aperfeiçoamento de Pessoal de Nível Superior (CAPES) and the Conselho Nacional de Desenvolvimento Científico e Tecnológico (CNPq) for the support. Thanks are given to the Brazilian Ministry of Science, Technology and Innovations (MCTI) and the Brazilian Space Agency (AEB). Cosme A. O. B. Figueiredo acknowledges FAPESP and the Fundação de apoio à pesquisa do estado da Paraíba. The authors thank the Estudo e Monitoramento Brasileiro do Clima Espacial (EMBRACE/INPE) for the provision of all-sky.

References

Bageston, J., Wrasse, C. M., Batista, P., Hibbins, R., Fritts, D., Gobbi, D., and Andrioli, V.: Observation of a mesospheric front in a thermal-doppler duct over King George Island, Antarctica, https://doi.org/10.5194/acp-11-12137-2011, 2011.

Becker, E. and Schmitz, G.: Climatological Effects of Orography and Land–Sea Heating Contrasts on the Gravity Wave–Driven Circulation of the Mesosphere, Journal of the Atmospheric Sciences, 60, 103 – 118, https://doi.org/10.1175/1520-0469(2003)060<0103:CEOOAL>2.0.CO;2, 2003.

Bowman, K. P.: An Introduction to Programming with IDL: Interactive data language, Elsevier, 2006.

Buriti, R., Takahashi, H., and Gobbi, D.: First results from mesospheric airglow observations at 7.5 º S., Revista Brasileira de Geofísica, 19, 169–176, 2001.

Chimonas, G. and Hines, C.: Doppler ducting of atmospheric gravity waves, Journal of Geophysical Research: Atmospheres, 91, 1219–1230, 1986.

Chou, M. Y., Lin, C. C., Yue, J., Tsai, H. F., Sun, Y. Y., Liu, J. Y., and Chen, C. H.: Concentric traveling ionosphere disturbances triggered by Super Typhoon Meranti (2016), Geophysical Research Letters, 44, 1219–1226, https://doi.org/doi:10.1002/2016GL072205, 2017.

Figueiredo, C., Takahashi, H., Wrasse, C., Otsuka, Y., Shiokawa, K., and Barros, D.: Investigation of nighttime MSTIDS observed by optical thermosphere imagers at low latitudes: Morphology, propagation direction, and wind filtering, Journal of Geophysical Research: Space Physics, 123, 7843–7857, https://doi.org/https://doi.org/10.1029/2018JA02543, 2018.

Figueiredo, C., Vadas, S., Becker, E., Wrasse, C., Takahashi, H., Nyassor, P., and Barros, D.: Secondary gravity waves from the Tonga volcano eruption: Observation and modeling over New Zealand and Australia, Journal of Geophysical Research: Space Physics, 128, e2023JA031 476, 2023.

Fritts, D. C. and Alexander, M. J.: Gravity wave dynamics and effects in the middle atmosphere, Reviews of geophysics, 41, https://doi.org/10.1029/2001RG000106, 2003.

Fritts, D. C., Janches, D., Riggin, D. M., Stockwell, R. G., Sulzer, M. P., and Gonzalez, S.: Gravity waves and momentum fluxes in the mesosphere and lower thermosphere using 430 MHz dual-beam measurements at Arecibo: 2. Frequency spectra, momentum fluxes, and variability, Journal of Geophysical Research: Atmospheres, 111, https://doi.org/10.1029/2005JD006883, 2006.

Gossard, E. E. and Hooke, W. H.: Waves in the atmosphere: atmospheric infrasound and gravity waves-their generation and propagation, Atmospheric Science, 2, 1975.

Heale, C. and Snively, J.: Gravity wave propagation through a vertically and horizontally inhomogeneous background wind, Journal of Geophysical Research: Atmospheres, 120, 5931–5950, https://doi.org/10.1002/2015JD023505, 2015.

Heale, C. J., Bossert, K., Vadas, S. L., Hoffmann, L., Dörnbrack, A., Stober, G., Snively, J., and Jacobi, C.: Secondary gravity waves generated by breaking mountain waves over Europe, Journal of Geophysical Research: Atmospheres, 125, e2019JD031 662, https://doi.org/10.1029/2019JD031662, 2020.

Holton, J. R.: The role of gravity wave induced drag and diffusion in the momentum budget of the mesosphere, Journal of Atmospheric Sciences, 39, 791–799, https://doi.org/10.1175/1520-0469(1982)039<0791:TROGWI>2.0.CO;2, 1982.

Innis, J. L., Phillips, F. A., Burns, G. B., Greet, P. A., French, W. J. R., and Dyson, P. L.: Mesospheric temperatures from observations of the hydroxyl (6–2) emission above Davis, Antarctica: A comparison of rotational and Doppler measurements, Annales Geophysicae, 19, 359–365, https://doi.org/10.5194/angeo-19-359-2001, 2001.

Isler, J. R., Taylor, M. J., and Fritts, D. C.: Observational evidence of wave ducting and evanescence in the mesosphere, Journal of Geophysical Research: Atmospheres, 102, 26 301–26 313, 1997.

Kaifler, N., Kaifler, B., Ehard, B., Gisinger, S., Dörnbrack, A., Rapp, M., Kivi, R., Kozlovsky, A., Lester, M., and Liley, B.: Observational indications of downward-propagating gravity waves in middle atmosphere lidar data, Journal of Atmospheric and Solar-Terrestrial Physics, 162, 16–27, 2017.

Kaifler, N., Kaifler, B., Dörnbrack, A., Rapp, M., Hormaechea, J. L., and de la Torre, A.: Lidar observations of large-amplitude mountain waves in the stratosphere above Tierra del Fuego, Argentina, Scientific reports, 10, 14 529, https://doi.org/https://doi.org/10.1038/s41598-020-71443-7, 2020.

Kogure, M., Yue, J., Nakamura, T., Hoffmann, L., Vadas, S. L., Tomikawa, Y., Ejiri, M. K., and Janches, D.: First Direct Observational Evidence for Secondary Gravity Waves Generated by Mountain Waves Over the Andes, Geophysical Research Letters, 47, e2020GL088 845, https://doi.org/10.1029/2020GL088845, 2020.

Kubota, M., Fukunishi, H., and Okano, S.: Characteristics of medium-and large-scale TIDs over Japan derived from OI 630-nm nightglow observation, Earth, planets and space, 53, 741–751, 2001.

Le Du, T., Keckhut, P., Hauchecorne, A., and Simoneau, P.: Observation of gravity wave vertical propagation through a mesospheric inversion layer, Atmosphere, 13, 1003, https://doi.org/10.3390/atmos13071003, 2022.

Li, Q., Xu, J., Liu, H., Liu, X., and Yuan, W.: How do gravity waves triggered by a typhoon propagate from the troposphere to the upper atmosphere?, Atmospheric Chemistry and Physics, 22, 12 077–12 091, https://doi.org/10.5194/acp-22-12077-2022, 2022.

Lima, L., Batista, P., Takahashi, H., and Clemesha, B.: Quasi-two-day wave observed by meteor radar at 22.7 S, Journal of atmospheric and solar-terrestrial physics, 66, 529–537, 2004.

Lindzen, R.: Gravity waves in the mesosphere, Dynamics of the middle atmosphere, pp. 3–18, 1984.

Lindzen, R. S.: Turbulence and stress owing to gravity wave and tidal breakdown, Journal of Geophysical Research: Oceans, 86, 9707–9714, https://doi.org/https://doi.org/10.1029/JC086iC10p09707, 1981.

Love, P. T. and Murphy, D. J.: Gravity wave momentum flux in the mesosphere measured by VHF radar at Davis, Antarctica, Journal of Geophysical Research: Atmospheres, 121, 12–723, https://doi.org/10.1002/2016JD025627, 2016.

Maekawa, R.: Observations of gravity waves in the mesopause region by multicolor airglow imaging, Master Thesis, Kyoto University, 2000.

Medeiros, A., Taylor, M. J., Takahashi, H., Batista, P., and Gobbi, D.: An investigation of gravity wave activity in the low-latitude upper mesosphere: Propagation direction and wind filtering, Journal of Geophysical Research: Atmospheres, 108, https://doi.org/https://doi.org/10.1029/2002JD002593, 2003.

Medvedev, A. S., Klaassen, G. P., and Yiğit, E.: On the dynamical importance of gravity wave sources distributed over different heights in the atmosphere, Journal of Geophysical Research: Space Physics, 128, e2022JA031 152, 2023.

Mies, F. H.: Calculated vibrational transition probabilities of OH (X2Π), Journal of Molecular Spectroscopy, 53, 150–188, 1974.

Nappo, C. J.: An introduction to atmospheric gravity waves, Academic press, 2013.

Narayanan, V. L., Wright, C., Mlynczak, M., Hindley, N., Kavanagh, A., Moffat-Griffin, T., and Noble, P.: Observations of mesospheric gravity waves generated by geomagnetic activity, Journal of Geophysical Research: Space Physics, 129, e2023JA032 157, 2024.

Nyassor, P. K., Buriti, R. A., Paulino, I., Medeiros, A. F., Takahashi, H., Wrasse, C. M., and Gobbi, D.: Determination of gravity wave parameters in the airglow combining photometer and imager data, in: Annales Geophysicae, vol. 36, pp. 705–715, Copernicus GmbH, https://doi.org/10.5194/angeo-36-705-2018, 2018.

Nyassor, P. K., Wrasse, C. M., Gobbi, D., Paulino, I., Vadas, S. L., Naccarato, K. P., Takahashi, H., Bageston, J. V., Figueiredo, C. A. O. B., and Barros, D.: Case Studies on Concentric Gravity Waves Source Using Lightning Flash Rate, Brightness Temperature and Backward Ray Tracing at São Martinho da Serra (29.44°S, 53.82°W), Journal of Geophysical Research: Atmospheres, 126, e2020JD034 527, https://doi.org/https://doi.org/10.1029/2020JD034527, 2021.

Nyassor, P. K., Wrasse, C. M., Paulino, I., Gobbi, D., Yiğit, E., Takahashi, H., Batista, P. P., Naccarato, K. P., Buriti, R. A., Paulino, A. R., Barros, D., and Figueiredo, C. A. O. B.: Investigations on Concentric Gravity Wave Sources Over the Brazilian Equatorial Region, Journal of Geophysical Research: Atmospheres, 127, e2021JD035 149, https://doi.org/https://doi.org/10.1029/2021JD035149, 2022a.

Nyassor, P. K., Wrasse, C. M., Paulino, I., São Sabbas, E. F., Bageston, J. V., Naccarato, K. P., Gobbi, D., Figueiredo, C. A., Ayorinde, T. T., Takahashi, H., et al.: Sources of concentric gravity waves generated by a moving mesoscale convective system in southern Brazil, Atmospheric Chemistry and Physics, 22, 15 153–15 177, https://doi.org/10.5194/acp-22-15153-2022, 2022b.

Paulino, I., Figueiredo, C. A. O. B., Rodrigues, F. S., Buriti, R. A., Wrasse, C. M., Paulino, A. R., Barros, D., Takahashi, H., Batista, I. S., Medeiros, A. F., Batista, P. P., Abdu, M. A., de Paula, E. R., Denardini, C. M., Lima, L. M., Cueva, R. Y., and Makela, J. J.: Atmospheric Gravity Waves Observed in the Nightglow Following the 21 August 2017 Total Solar Eclipse, Geophysical Research Letters, 47, e2020GL088 924, https://doi.org/https://doi.org/10.1029/2020GL088924, 2020.

Roach, F. E.: The light of the night sky, vol. 8, Springer Science & Business Media, 2013.

Sato, K. and Yoshiki, M.: Gravity wave generation around the polar vortex in the stratosphere revealed by 3-hourly radiosonde observations at Syowa Station, Journal of the Atmospheric Sciences, 65, 3719–3735, https://doi.org/10.1175/2008JAS2539.1, 2008.

Schöch, A., Baumgarten, G., Fritts, D., Hoffmann, P., Serafimovich, A., Wang, L., Dalin, P., Müllemann, A., and Schmidlin, F.: Gravity waves in the troposphere and stratosphere during the MaCWAVE/MIDAS summer rocket program, Geophysical research letters, 31, https://doi.org/10.1029/2004GL019837, 2004.

Sentman, D., Wescott, E., Picard, R., Winick, J., Stenbaek-Nielsen, H., Dewan, E., Moudry, D., Sao Sabbas, F., Heavner, M., and Morrill, J.: Simultaneous observations of mesospheric gravity waves and sprites generated by a midwestern thunderstorm, Journal of Atmospheric and Solar-Terrestrial Physics, 65, 537–550, https://doi.org/10.1016/S1364-6826(02)00328-0, 2003.

Silverman, S.: Night airglow phenomenology, Space Science Reviews, 11, 341–379, 1970.

Sivjee, G. and Hamwey, R.: Temperature and chemistry of the polar mesopause OH, Journal of Geophysical Research: Space Physics, 92, 4663–4672, 1987.

Snively, J. B. and Pasko, V. P.: Excitation of ducted gravity waves in the lower thermosphere by tropospheric sources, Journal of Geophysical Research: Space Physics, 113, https://doi.org/10.1029/2007JA012693, 2008.

Snively, J. B., Pasko, V. P., Taylor, M. J., and Hocking, W. K.: Doppler ducting of short-period gravity waves by midlatitude tidal wind structure, Journal of Geophysical Research: Space Physics, 112, https://doi.org/10.1029/2006JA011895, 2007.

Suzuki, S., Shiokawa, K., Otsuka, Y., Ogawa, T., Kubota, M., Tsutsumi, M., Nakamura, T., and Fritts, D. C.: Gravity wave momentum flux in the upper mesosphere derived from OH airglow imaging measurements, Earth, planets and space, 59, 421–428, 2007.

Suzuki, S., Lübken, F.-J., Baumgarten, G., Kaifler, N., Eixmann, R., Williams, B. P., and Nakamura, T.: Vertical propagation of a mesoscale gravity wave from the lower to the upper atmosphere, Journal of Atmospheric and Solar-Terrestrial Physics, 97, 29–36, https://doi.org/10.1016/j.jastp.2013.01.012, 2013.

Takahashi, H., Batista, P. P., Buriti, R., Gobbi, D., Nakamura, T., Tsuda, T., and Fukao, S.: Simultaneous measurements of airglow oh emissionand meteor wind by a scanning photometer and the muradar, Journal of atmospheric and solar-terrestrial physics, 60, 1649–1668, 1998.

Taori, A., Taylor, M. J., and Franke, S.: Terdiurnal wave signatures in the upper mesospheric temperature and their association with the wind fields at low latitudes (20 N), Journal of Geophysical Research: Atmospheres, 110, https://doi.org/10.1029/2004JD004564, 2005.

Taylor, M. J. and Hapgood, M.: Identification of a thunderstorm as a source of short period gravity waves in the upper atmospheric nightglow emissions, Planetary and space science, 36, 975–985, https://doi.org/10.1016/0032-0633(88)90035-9, 1988.

Townsend, A.: Internal waves produced by a convective layer, Journal of Fluid Mechanics, 24, 307–319, https://doi.org/10.1017/S0022112066000661, 1966.

Vadas, S. L.: Horizontal and vertical propagation and dissipation of gravity waves in the thermosphere from lower atmospheric and thermospheric sources, Journal of Geophysical Research: Space Physics, 112, https://doi.org/10.1029/2006JA011845, 2007.

Vadas, S. L., Fritts, D. C., and Alexander, M. J.: Mechanism for the generation of secondary waves in wave breaking regions, Journal of the Atmospheric Sciences, 60, 194–214, https://doi.org/10.1175/1520-0469(2003)060<0194:MFTGOS>2.0.CO;2, 2003.

Vadas, S. L., Taylor, M. J., Pautet, P.-D., Stamus, P., Fritts, D. C., Liu, H.-L., São Sabbos, F., Batista, V., Takahashi, H., and Rampinelli, V.: Convection: the likely source of the medium-scale gravity waves observed in the OH airglow layer near Brasilia, Brazil, during the SpreadFEx campaign, in: Annales Geophysicae, vol. 27, p. 231, European Geosciences Union, https://doi.org/10.5194/angeo-27-231-2009, 2009.

Vadas, S. L., Zhao, J., Chu, X., and Becker, E.: The excitation of secondary gravity waves from local body forces: Theory and observation, Journal of Geophysical Research: Atmospheres, 123, 9296–9325, https://doi.org/10.1029/2017JD027970, 2018.

Vargas, F., Swenson, G., Liu, A., and Gobbi, D.: O (1S), OH, and O2 (b) airglow layer perturbations due to AGWs and their implied effects on the atmosphere, Journal of Geophysical Research: Atmospheres, 112, 2007.

Vargas, F., Gobbi, D., Takahashi, H., and Lima, L.: Gravity wave amplitudes and momentum fluxes inferred from OH airglow intensities and meteor radar winds during SpreadFEx, in: Annales Geophysicae, vol. 27, pp. 2361–2369, Copernicus Publications Göttingen, Germany, 2009.

Wrasse, C. M., Takahashi, H., and Gobbi, D.: Comparison of the OH (8-3) and (6-2) band rotational temperature of the mesospheric airglow emissions, Revista Brasileira de Geofísica, 22, 223–231, https://doi.org/10.1590/S0102-261X2004000300002, 2004.

Wrasse, C. M., Takahashi, H., Medeiros, A. F., Lima, L. M., Taylor, M. J., Gobbi, D., and Fechine, J.: Determinaçao dos parâmetros de ondas de gravidade através da análise espectral de imagens de aeroluminescência, Revista Brasileira de Geofísica, 25, 257–265, https://doi.org/10.1590/S0102-261X2007000300003, 2007.

Wrasse, C. M., Nyassor, P. K., da Silva, L. A., Figueiredo, C. A., Bageston, J. V., Naccarato, K. P., Barros, D., Takahashi, H., and Gobbi, D.: Studies on the propagation dynamics and source mechanism of quasi-monochromatic gravity waves observed over São Martinho da Serra (29° S, 53° W), Brazil, Atmospheric Chemistry and Physics, 24, 5405–5431, 2024.

Yamashita, C., Chu, X., Liu, H.-L., Espy, P. J., Nott, G. J., and Huang, W.: Stratospheric gravity wave characteristics and seasonal variations observed by lidar at the South Pole and Rothera, Antarctica, Journal of Geophysical Research: Atmospheres, 114, https://doi.org/10.1029/2008JD011472, 2009.

Yiğit, E. and Medvedev, A. S.: Heating and cooling of the thermosphere by internal gravity waves, Geophysical Research Letters, 36, 2009.

Yiğit, E. and Medvedev, A. S.: Role of gravity waves in vertical coupling during sudden stratospheric warmings, Geoscience Letters, 3, 1–13, https://doi.org/https://doi.org/10.1186/s40562-016-0056-1, 2016.

Yiğit, E., Aylward, A. D., and Medvedev, A. S.: Parameterization of the effects of vertically propagating gravity waves for thermosphere general circulation models: Sensitivity study, Journal of Geophysical Research: Atmospheres, 113, 2008.

Yiğit, E., Knížová, P. K., Georgieva, K., and Ward, W.: A review of vertical coupling in the Atmosphere–Ionosphere system: Effects of waves, sudden stratospheric warmings, space weather, and of solar activity, Journal of Atmospheric and Solar-Terrestrial Physics, 141, 1–12, 2016.

Yiğit, E., Medvedev, A. S., and Ern, M.: Effects of latitude-dependent gravity wave source variations on the middle and upper atmosphere, Frontiers in Astronomy and Space Sciences, 7, 614 018, 2021.

Yue, J., Vadas, S. L., She, C.-Y., Nakamura, T., Reising, S. C., Liu, H.-L., Stamus, P., Krueger, D. A., Lyons, W., and Li, T.: Concentric gravity waves in the mesosphere generated by deep convective plumes in the lower atmosphere near Fort Collins, Colorado, Journal of Geophysical Research: Atmospheres, 114, https://doi.org/10.1029/2008JD011244, 2009.

Yue, J., Miller, S. D., Straka III, W. C., Noh, Y.-J., Chou, M.-Y., Kahn, R., and Flower, V.: La Soufriere volcanic eruptions launched gravity waves into Space, Geophysical Research Letters, 49, e2022GL097 952, https://doi.org/10.1029/2022GL097952, 2022.